Title

A discrete element method representation of an anisotropic elastic continuum

Permalink

Authors

Truszkowska, Agnieszka
Yu, Qin
Greaney, P Alex
et al.

Publication Date

DOI

Peer reviewed

Accepted Manuscript

A Discrete Element Method Representation of an Anisotropic Elastic Continuum

Agnieszka Truszkowska , Qin Yu , P. Alex Greaney ,
T. Matthew Evans , Jaime J. Kruzic

Please cite this article as: Agnieszka Truszkowska , Qin Yu , P. Alex Greaney , T. Matthew Evans , Jaime J. Kruzic , A Discrete Element Method Representation of an Anisotropic Elastic Continuum, *Journal of the Mechanics and Physics of Solids* (2018), doi: 10.1016/j.jmps.2018.04.015

A Discrete Element Method Representation of an Anisotropic Elastic Continuum

Agnieszka Truszkowska[a,b], Qin Yu[a], P. Alex Greaney[c,*],

T. Matthew Evans[b,*], Jaime J. Kruzic[d]

[a]*School of Mechanical, Industrial, & Manufacturing Engineering, Oregon State University, Corvallis, OR 97331, USA*

[b]*School of Civil & Construction Engineering, Oregon State University, Corvallis, OR 97331, USA*

[c]*Mechanical Engineering Department, University of California — Riverside, Riverside, CA 92501, USA*

[d] *School of Mechanical and Manufacturing Engineering, UNSW Sydney, NSW 2052, Australia*

ABSTRACT

A method for modeling cubically anisotropic elasticity within the discrete element method is presented. The discrete element method (DEM) is an approach originally intended for modeling granular materials (sand, soil, and powders); however, recent developments have usefully extended it to model stochastic mechanical processes in monolithic solids which, to date, have been assumed to be elastically isotropic. The method presented here for efficiently capturing cubic elasticity in DEM is an important prerequisite for further extending DEM to capture the influence of elastic anisotropy on the mechanical response of polycrystals, composites, etc. The system demonstrated here uses a directionally assigned stiffness in the bonds between adjacent elements and includes separate schemes for achieving anisotropy with Zener ratios greater and smaller than one. The model framework is presented along with an analysis of the accessible space of elastic properties that can be modeled and an artificial neural network interpolation scheme for mapping input parameters to model elastic behavior.

Keywords: discrete element method, anisotropic elasticity, granular mechanics

1   INTRODUCTION

The discrete element method (DEM) is a well-established computational framework originally developed for modeling granular materials (Cundall and Strack, 1979). In DEM, the discrete granular constituents of a material (in two or three dimensions) are represented with discrete geometric elements, e.g., spheres, ellipsoids, or polyhedra. The material is modeled through relatively simple interactions between the elements and does not rely on overarching constitutive relations to predict bulk material response. DEM is particularly attractive because one can accurately model deformation of the material, including its failure, with only a minimal amount of assumptions and input parameters.

DEM modeling has been successful for modeling a wide range of phenomena in both loose and bound granular materials (Zhu et al., 2007, 2008), including deformation (Evans and Frost, 2010; Johnson and Hopkin, 2005), microstructure evolution (Evans and Valdes, 2011; Jacobson et al., 2007), fracture (Fakhimi et al., 2002; Lobo-Guerrero and Vallejo, 2005; Potyondy and Cundall, 2004), creep (Wang et al., 2008), and sintering (Martin et al., 2009). Building on the successes for granular materials, more recently there have been efforts in applying DEM to modeling mechanical properties of isotropic solids, such as glasses and polymers, that have been traditionally modeled as continua (Andre et al., 2013; Hedjazi et al., 2012; Jebahi et al., 2013; Kosteski et al., 2012). Modelling solids using DEM involves bonding the discrete elements together at their contact points and the main motivation is to exploit several attractive features of DEM. For example, DEM models naturally capture spatial heterogeneity and discontinuous deformations and are particularly well-suited for simulation of emergent phenomena such as inhomogeneous localization of deformation (e.g., shear band, void, or crack formation).

The initial development of DEM models for solid materials has primarily focused on the fracture behavior of *elastically isotropic and homogeneous* solids such as brittle polymers (Hedjazi et al., 2012; Kosteski et al., 2012) and silica glass (Andre et al., 2013; Jebahi et al., 2013). More recent work has involved the development of DEM models for fiber reinforced polymer composites where the overall composite is anisotropic and inhomogeneous, but each constituent is considered as isotropic (Le et al., 2016; Maheo et al., 2015). Anisotropy naturally emerges when a uniaxial fiber orientation is used; however, as noted by (Maheo et al., 2015) carbon fibers are inherently anisotropic at the constituent level and those researchers left the incorporation of fiber anisotropy for future work. Similarly, researchers have developed isotropic DEM models to simulate the fatigue failure of metals (Hahn et al., 2013); however, the metal microstructure and the cubic elastic anisotropy were not considered.

As mentioned above, a key strength of DEM modelling is its ability to capture emergent damage phenomena and microstructure evolution in granular materials. It has been suggested that for DEM to achieve similar success for modelling solid materials with inherent elastic anisotropy, that local anisotropy must be included to achieve the correct physics of the damage phenomena (Truszkowska et al., 2017). Accordingly, this work represents a first step in adapting DEM to model solid materials with cubic crystal anisotropy, including many metal alloys and

2

ceramics. In this approach, cubic elastic anisotropy is imposed on a bonded assembly of spherical discrete elements by defining the bond stiffnesses with spheroidal-shaped, orientation-dependent distributions that ensure the correct symmetry of the elastic stiffness tensor. While not suitable for all cubic materials, the results presented herein demonstrate that this method can be used for numerous real cubic materials with small to moderate anisotropy ratios.

2   THEORETICAL FOUNDATION OF THE DISCRETE ELEMENT METHOD

The discrete element method was originally developed by (Cundall, 1971) for the modeling of rocks and later expanded to soils (Cundall and Strack, 1979). In this introduction, we present major points of the method, while for details of the implementation the reader is referred to (Potyondy and Cundall, 2004). In this work, the three-dimensional version of the DEM with spherical elements is employed.

Traditional DEM is predicated upon the simultaneous solution of Newton's equations of motion for each body in an assembly of discrete particles. Contacting particles interact via simple constitutive relations. Particle overlap is allowed at contacts (the so-called *soft contact* approach), but these overlaps are small relative to particle size (e.g., less than 1%). A given calculation cycle begins by identifying contact points and identifying their unit normals.

Figure 1 shows two interacting spherical elements and an element interacting with a rigid planar wall. The contact plane normal ($\mathbf{n_c}$) is defined by the line segment between the element centroids $\mathbf{x_{p_i}}$ or element centroid and nearest point on the wall, $\mathbf{x_w}$. The contact plane spans the contact point $\mathbf{x_c}$. **N.B.:** In DEM modeling, contacts may be either *real* or *virtual*. Real contacts occur when two bodies are actually in contact or overlapping. Virtual contacts exist when two bodies are proximal but not yet touching (typically, when their surface separation is 10^{-6} times the mean diameter of the two entities). In unbonded assemblies, this serves to provide computational efficiency in the contact detection algorithm (typically the most expensive part of the calculation). In bonded assemblies, however, this separation has physical meaning – two elements are able to have a physical separation, yet still be connected via a bond between them.

Herein, the behavior of elements contacts is described by a linear contact law. The normal force between two contacting elements is given by $F = -kx$ where k is particle stiffness and x is contact overlap. If the two elements are bonded (as they are in this work), an additional normal force is generated due to the presence of the bond, as described subsequently. Shear forces at contacts are linear and formulated incrementally.
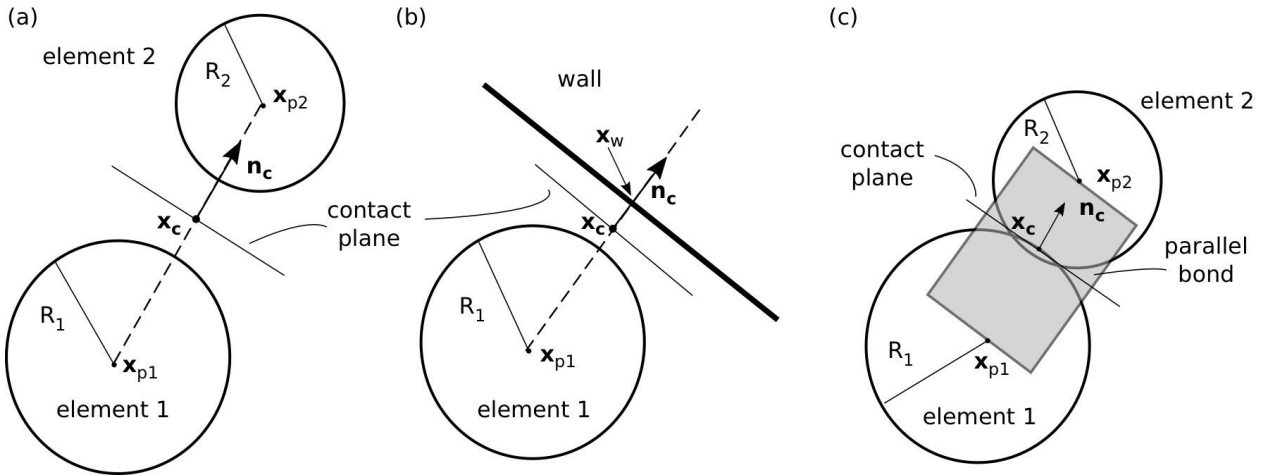
3

Figure 1: DEM components: (a) two interacting elements, (b) an element interacting with a wall, and (c) two elements bonded with a parallel bond.

The resultant force (and subsequently, the equation of motion) for a single element is defined as:

$$\mathbf{F} = \sum_{i=1}^{N_c} \mathbf{F}_{ci} = m\mathbf{a},$$ (1)

where the total force $\boldsymbol{F}$ is the sum of forces $\boldsymbol{F}_{ci}$ due to the ith neighboring element; N_c is the total number of contacts the element has formed, m is element mass, and $\mathbf{a}$ is the acceleration. Similarly, the total moment, $\boldsymbol{M}$, experienced by an element is:

$$\mathbf{M} = \sum_{i=1}^{N_c} \mathbf{M}_{ci} = I\dot{\boldsymbol{\omega}} = \left(\frac{2}{5}mR^2\right)\dot{\boldsymbol{\omega}},$$ (2)

where $\boldsymbol{M}_{ci}$ is the moment on the ith element contact, I is the moment of inertia, $\dot{\boldsymbol{\omega}}$ is the angular acceleration, and we exploit the fact that, for spherical elements, moment is directionally independent. Each contact force $\boldsymbol{F}_{ci}$ and moment, $\boldsymbol{M}_{ci}$, is resolved into a normal component acting along the contact plane normal, $\boldsymbol{n}_c$, and shear component that lies in the plane. As mentioned previously, in simulations of unbound granular materials forces are related to the overlap of impinging elements as shown in Figure 1. Positive overlap generates repulsive force. This sign convention is natural for unbonded materials where contacts only work in compression and so there are no tensile forces, but it is the reverse of the convention typically used in solid mechanics.

To model monolithic materials, elements can be bonded together by replacing the asymmetrical contact laws with cohesive interactions that can support tension. A common scheme for this is the *parallel bond* developed by Potyondy an Cundall (2004) and shown in Figure 1(c). The parallel bond represents two welded elements as a cylinder of material

4

running between the element centers that can transmit both moment and force between the elements. The constitutive law for the parallel bond is used in the differential form:

$$\frac{d\mathbf{F}}{dt} = k_n A \frac{d\mathbf{u}_n}{dt} + k_s A \frac{d\mathbf{u}_s}{dt}$$
$$\frac{d\mathbf{M}}{dt} = -k_n J \frac{d\Delta\theta_t}{dt} - k_s I \frac{d\Delta\theta_b}{dt}$$

(3)

where the force, $\boldsymbol{F}$, due to the normal, $\boldsymbol{u}_n$, and shear, $\boldsymbol{u}_s$, displacements, and the moment, $\boldsymbol{M}$, due to the difference in the twisting, $\Delta\boldsymbol{\theta}_t$, and bending, $\Delta\boldsymbol{\theta}_t$, rotations of the two elements are related by normal, k_n, and shear stiffness, k_s. The geometric terms A, I, and J are the bond's cross-sectional area, moment of inertia, and polar moment of inertia, respectively. For unbonded elements the interaction range is set by the element radii, as discussed previously. Parallel bonds, however, can be installed between any two elements with any equilibrium length, and thus once a DEM assembly is parallel bonded the elements should no longer be considered to be spherical. In this work, assemblies of elements were generated by simulating the dynamic packing of unbonded elements interacting through contact laws. Once a stable packing was achieved, the element-element contact laws were turned off and parallel bonds installed between all pairs of elements with a spacing less than a cutoff separation referred to as the *gap parameter*, $g_{c_{\max}}$, so that a bond is installed between elements *i* and *j* if:

$$g_{c_{\max}} \geq \left\| \mathbf{x}_{p2} - \mathbf{x}_{p1} \right\| - \left(R_1 + R_2\right)$$

(4)

where $\boldsymbol{x}_{p1}$ and $\boldsymbol{x}_{p2}$ are positions of the elements' centroids and R_1 and R_2 the element radii (Figure 1). In this work, the geometric terms A, I, and J are defined by the bond radius which is defined as the radius of the smaller element, $R_b = min\{R^{(1)}, R^{(2)}\}$ or the radius of the element at an element-wall contact.

Each simulation step in DEM consists of computing the total forces and moments for every element using Eq.1 and 2. From these, accelerations, translational and angular velocities, and new element positions are computed with the Verlet algorithm (Verlet, 1967).

3   INTRODUCTION OF CUBIC CRYSTAL ANISOTROPY IN DEM

The elastic response of cubically symmetric crystals is defined by the fourth rank elastic stiffness tensor with three independent moduli C_{11}, C_{12}, and C_{44} to provide the following stress-strain relationship:

$$\begin{pmatrix} \sigma_{xx} \\ \sigma_{yy} \\ \sigma_{zz} \\ \sigma_{yz} \\ \sigma_{xz} \\ \sigma_{xy} \end{pmatrix} = \begin{pmatrix} C_{11} & C_{12} & C_{12} & 0 & 0 & 0 \\ C_{12} & C_{11} & C_{12} & 0 & 0 & 0 \\ C_{12} & C_{12} & C_{11} & 0 & 0 & 0 \\ 0 & 0 & 0 & C_{44} & 0 & 0 \\ 0 & 0 & 0 & 0 & C_{44} & 0 \\ 0 & 0 & 0 & 0 & 0 & C_{44} \end{pmatrix} \begin{pmatrix} \varepsilon_{xx} \\ \varepsilon_{yy} \\ \varepsilon_{zz} \\ \varepsilon_{yz} \\ \varepsilon_{xz} \\ \varepsilon_{xy} \end{pmatrix} \tag{5}$$

This relatively simple expression belies that cubically symmetric materials have a complex directionally dependent deformational response to a load. To present the rationale behind the approach set forth here for replicating this within DEM, it is necessary to describe the subtleties of cubic anisotropy in more depth. The extra variable needed to describe elastic response of cubic materials over isotropic media is often expressed as the Zener anisotropy ratio, $Z = \frac{2C_{44}}{C_{11} - C_{12}}$. This describes a material's deviation from isotropic behavior with a ratio of one indicating that the material is isotropic. Figure 2 shows the directionally dependent stiffness of three cubic materials with Z ranging from less than one to greater than one. The materials' stiffness in response to a uniaxial normal load varies with crystal loading direction (the left most plot in each sequence in Figure 2). Moreover, on any surface the material will have a hard and soft direction of shear. These soft and firm shear stiffnesses are plotted in the second and third plots in each sequence, respectively. The right-most plots show the soft and stiff shear stiffnesses overlaid, demonstrating that the soft and stiff shear stiffnesses are degenerate on the high symmetry {100} and {111} planes. In these plots, it can be seen that materials with an anisotropy ratio $Z < 1$ have the largest normal stiffness along $\langle 100 \rangle$ direction and the highest shear stiffness on {111} planes, while materials with $Z > 1$ have the largest normal stiffness along $\langle 111 \rangle$ direction and largest shear stiffness on {100}.
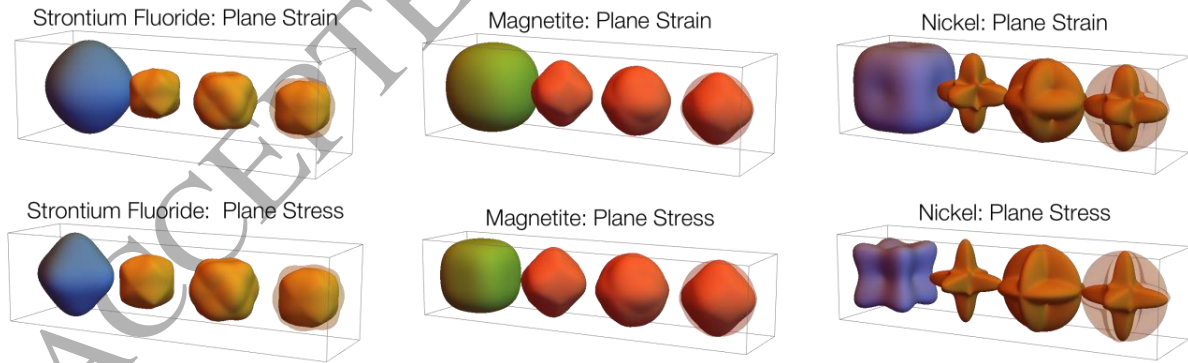

Figure 2: Elastic indicatrix for strontium fluoride, magnetite, and nickel. In each plot, the left most plot is the directionally dependent stiffness of the materials in response to a normal stress. The middle two plots show the shear stiffness along the soft and stiff shear directions on the plane normal to the polar direction, and the right most plot shows these shear stiffnesses overlaid. In the upper plots (labeled "Plane Strain") the stiffness is in response to an imposed uniaxial normal or in-plane shear strain while keeping the other strains values at zero, and the lower plots labeled "Plane Stress" are the stiffnesses in response to an imposed uniaxial normal or in-plane shear stress while keeping the other stress values at zero. In all plots, the values of

stiffness are plotted scaled by the materials' C11. The Zener ratios for strontium fluorite, magnetite and nickel are 0.78, 1.22, and 2.64, respectively. As the Zener ratio transitions from less than to greater than one, the materials' stiff axis transitions from ⟨100⟩ to ⟨111⟩.

The goal of this work is to capture cubic elasticity in DEM using the parallel bond formalism that is already implemented in many DEM software packages. In these packages, the user may assign a normal and shear stiffness for individual parallel bonds and thus the task becomes determining a method for assigning these stiffnesses based on bonds' *initial* orientations relative to a set of imagined crystallographic axes such that the emergent collective response of the bonded assembly is described by the stiffness tensor in Equation 5.

As the packing of elements in DEM is random, and *on average* isotropic, it is presumed that the cubic response must arise from the collective behavior of the assembly rather than being met at each individual element. Within this approach there are three steps of reasoning that can be used guide the selection of a directionally dependent function for assigning bond stiffnesses: From von Neumann's principle, the angular dependence of the stiffness distribution must possess cubic symmetry, that is, four axes of threefold rotational symmetry about the <111> directions of the imagined crystal. Second, the stiffness tensor in Equation 5 possesses only three independent variables, of which only one describes the deviation from isotropic elasticity. With only one degree of anisotropy it is conjectured that *any* angular stiffness function with the proper rotational symmetry could give rise to collective behavior that is cubically anisotropic. Finally, in cubic materials there is a qualitative change in the directionally dependent normal stiffness as the Zener anisotropy ratio, Z, transitions from smaller to greater than one. As can be seen in Figure 2, for Z<1 the normal stiffness is maximal along <100>, while for Z>1 the modulus is stiffest along <111>. It is therefore presumed that changing the angular distribution of parallel bond stiffnesses from being maximal along <111> to maximal along <100> will alter the direction a system's deviation from isotropic elasticity.

To meet these criteria, one could construct angular bond stiffness functions from a sum of suitably symmetrized spherical harmonics functions, and then iterate the shape of the angular distribution to explore the angular function space. However, rather than doing this, the goal of this article is to present a proof of concept that DEM can be used to model cubically elastic media. To this end, a more pragmatic approach was chosen, with two very simple piecewise functions defined as the external surface of a set of overlapping prolate spheroids (as shown in Figure 3). The shape of the distribution is described by a single parameter *a* that describes the aspect ratio (major to minor axes) of a family of spheroid with constant volume. One function is maximal along <100> and is composed of three spheroids with major axes along the <100> directions, while the second function, maximal along <111>, is composed of 4 co-centered spheroids with principal axes along the four <111> directions. In each case the spheroids the stiffness along a direction is given by the maximum radius of the three or four spheroids in which the radius is given by the equations:

$$k(\mathbf{n}, a) = k_0 (A/L) r_m(\mathbf{n}, a) \tag{6}$$

7

$$k_0\left(A/L\right) = \frac{A_b}{L_b}k_l \tag{7}$$

and the dimensionless parameter

$$r_m\left(\mathbf{n},a\right) = \max\left(\left\{r_1, r_2, ..., r_N\right\}\right) \tag{8}$$

$\mathbf{n}$ is the initial contact normal direction, A_b is the bond area, L_b the bond length, and k_l the stiffness magnitude. Bond length is defined as the sum of element radiuses, $L_b = R_1 + R_2$. N indicates the number of spheroids – 3 or 4 in this work. For the case of $N=3$ spheroids aligned along $\langle 100 \rangle$:

$$r_{i1} = \frac{a_i^{\frac{2}{3}}}{\sqrt{n_x^2 + \left(n_y^2 + n_z^2\right)a_i^2}} \tag{9}$$

$$r_{i2} = \frac{a_i^{\frac{2}{3}}}{\sqrt{n_y^2 + \left(n_x^2 + n_z^2\right)a_i^2}} \tag{10}$$

$$r_{i3} = \frac{a_i^{\frac{2}{3}}}{\sqrt{n_z^2 + \left(n_y^2 + n_x^2\right)a_i^2}} \tag{11}$$

where n_x, n_y, and n_z are the x, y, and z components of unit vector $\mathbf{n}$. For the case of $N=4$ spheroids aligned along $\langle 111 \rangle$ the spheroid radii are given by:

$$r_{j1} = \frac{a_j^{\frac{2}{3}}}{\sqrt{\frac{1}{3}\left[\left(n_x - n_y + n_z\right)^2 + 2\left(n_x^2 + n_x n_y + n_y^2 - n_x n_z + n_y n_z + n_z^2\right)a_j^2\right]}} \tag{12}$$

$$r_{j2} = \frac{a_j^{\frac{2}{3}}}{\sqrt{\frac{1}{3}\left[\left(n_x + n_y - n_z\right)^2 + 2\left(n_x^2 - n_x n_y + n_y^2 + n_x n_z + n_y n_z + n_z^2\right)a_j^2\right]}} \tag{13}$$

$$r_{j3} = \frac{a_j^{\frac{2}{3}}}{\sqrt{\frac{1}{3}\left[\left(-n_x + n_y + n_z\right)^2 + 2\left(n_x^2 + n_x n_y + n_y^2 + n_x n_z - n_y n_z + n_z^2\right)a_j^2\right]}} \tag{14}$$

$$r_{j4} = \frac{a_j^{\frac{2}{3}}}{\sqrt{\frac{1}{3}\left[\left(n_x + n_y + n_z\right)^2 + 2\left(n_x^2 - n_x n_y + n_y^2 - n_x n_z - n_y n_z + n_z^2\right)a_j^2\right]}} \tag{15}$$

In this way, the anisotropic behavior of the DEM model is controlled by three independent tuning parameters: a_n and a_s, the anisotropy in the system of spheroids used to assign the normal and shear stiffnesses, respectively, and $a_k = k_n/k_s$, the ratio of the normal and shear stiffness magnitudes. In Appendix A, a general analytic model is presented for determining the elastic moduli of a material with angularly dependent stiffness functions if the bonds are all deformed uniformly due to a homogeneous deformation of the assembly. In Appendix B, the model is used to prove that that the stiffness functions based on overlapping spheroids (Eqs. 5-14) result in cubically anisotropic elasticity.

The expression chosen to represent the spheroids has the property of describing spheroids of constant volume independent of a. In exploring the space of model parameters, it is useful to define log normalized parameters α as the log of a shifted and scaled parameter that varies from 0 to 1 so that generally

$$\alpha = \frac{\log(a) - \log(a_{\min})}{\log(a_{\max}) - \log(a_{\min})} \tag{16}$$

The plots in Figure 3 show the angular dependence of normal stiffness (blue) and shear stiffness (gold) assigned to parallel bonds in the Z<1 and Z>1 models at the vertices of the domain of log-normalized model parameters. In this work, only the space of model parameters was explored with a_n and a_s running from 0.022 to 5 and a_k ranging from 0.005 to 1. Parameters outside this range would lead to unrealistically exaggerated shapes of the spheroid distributions. These extreme limiting shapes are shown on Figure 3 and include cases where the shear stiffness becomes much smaller than the normal stiffness or the spheroid distribution becomes very narrow and pointy along its major directions.
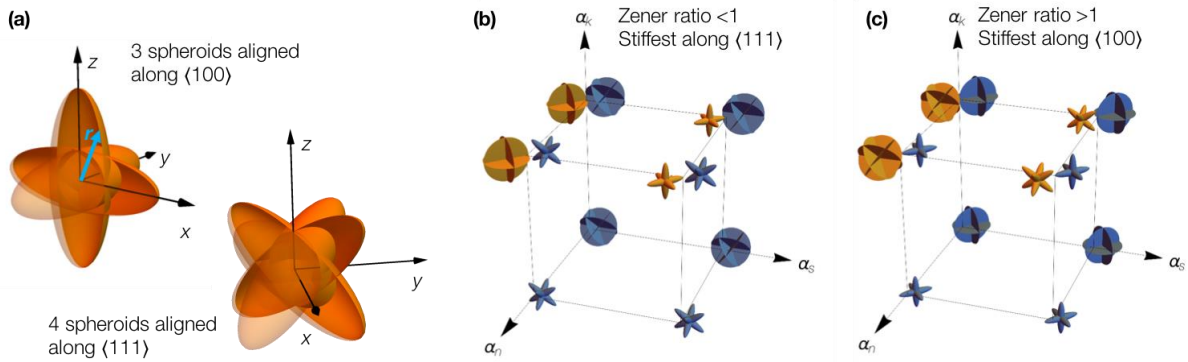
9

Figure 3: (a) Shows two piecewise angular functions with cubic symmetry defined as the outer surface of overlapping spheroids. The upper left function is constructed from three identical spheroids with major axes along the ⟨100⟩ directions and the the function of the lower right is formed by four identical spheroids with major axes along the ⟨111⟩ directions. (b & c) The angular distributions of parallel bond normal stiffness (blue) and shear stiffness (gold) as a function of the model parameters a_n, a_s, and a_k plotted on the normalized log scale (see text for explanation). In this space α_n, and α_s span from 0.029 to 3.5 and α_k spans 0.078 to 5.5. Figure (b) is for modeling materials with Z<1 which are stiffest along the ⟨100⟩ directions and so the normal stiffness is represented by three spheroids aligned along these directions. Figure (c) shows stiffness distributions for modeling materials with Z>1 which are stiffest along the ⟨111⟩ directions, and so the normal stiffness is represented by four spheroids aligned along these directions.

4   METHODS

4.1   Generating and Deforming an Element Assembly

Element assemblies were generated by randomly positioning elements in a cubical space until a predefined void fraction of 0.40 was achieved. The void fraction was selected to be approximately halfway between the best estimates for the random close pack (RCP) case of 0.36 and the jamming transition of 0.44 where an unbonded assembly will become unstable and readily flow. Element radii were randomly drawn from a uniform distribution with a range $\Delta R = \bar{R}/6$ where $\bar{R}$ is the arithmetic mean element radius.

Mass-scaling was employed to improve calculation speed; in this approach, element sizes are increased by several orders of magnitude to increase the critical time step for numerical stability (see, e.g., (Belheine et al., 2009; Evans and Frost, 2007; Ning et al., 2015; Yun and Evans, 2011; Zhao et al., 2017)). Simulations were performed in the absence of gravity so that the increased element sizes do not generate excessive self-weight within the assembly. Changing the particle size also affects the dimensionless inertial number, I, which is used to define the line of demarcation between quasi-static and dynamic simulations (Roux and Chevoir, 2005): $I = \dot{\gamma}d/\sqrt{P/\rho}$, where $\dot{\gamma}$ is strain rate, d is element diameter, P is pressure, and ρ is particle density. Simulations with an inertial number less than 10^{-3} are quasi-static. In the current work the average inertial number is lower than 5×10^{-4}.

After the model domain was randomly populated with elements the system was relaxed by simulating the evolution of the system with damped dynamics until element accelerations are

10

minimized. After equilibration, all neighboring elements within a chosen cutoff distance (called the gap cutoff parameter, $g_{c,\,max}$) were fused together with parallel bonds to form a contiguous network, and then the bounding walls were removed. Stress equilibration is not necessary as once parallel bonds are installed the elements' contact stiffnesses are removed. At this point the elements cease to be particle-like and are instead a trellis of *bonds*, all initially fully relaxed with no internal forces or moments. The total number of bonds formed is a function of the gap cutoff parameter. If the gap between elements is smaller than the predefined gap parameter, $g_{c,\,max}$, a bond will form between these elements. The influence of the gap cutoff parameter on the bonded network, the element coordination number, and the resulting elastic response was verified for a number of gap cutoff parameter values from $1.7\mathrm{x}10^{-4}\,\bar{R}$ to $0.8\,\bar{R}$.

The stiffnesses of individual bonds were assigned based on the bonds' initial orientation according to the spheroid distributions described in Eqs. 6–15n. Elements that were initially bonded to box walls were used as "grip elements" to apply the elastic deformation, as discussed subsequently. A typical assembly is shown in Figure 4.
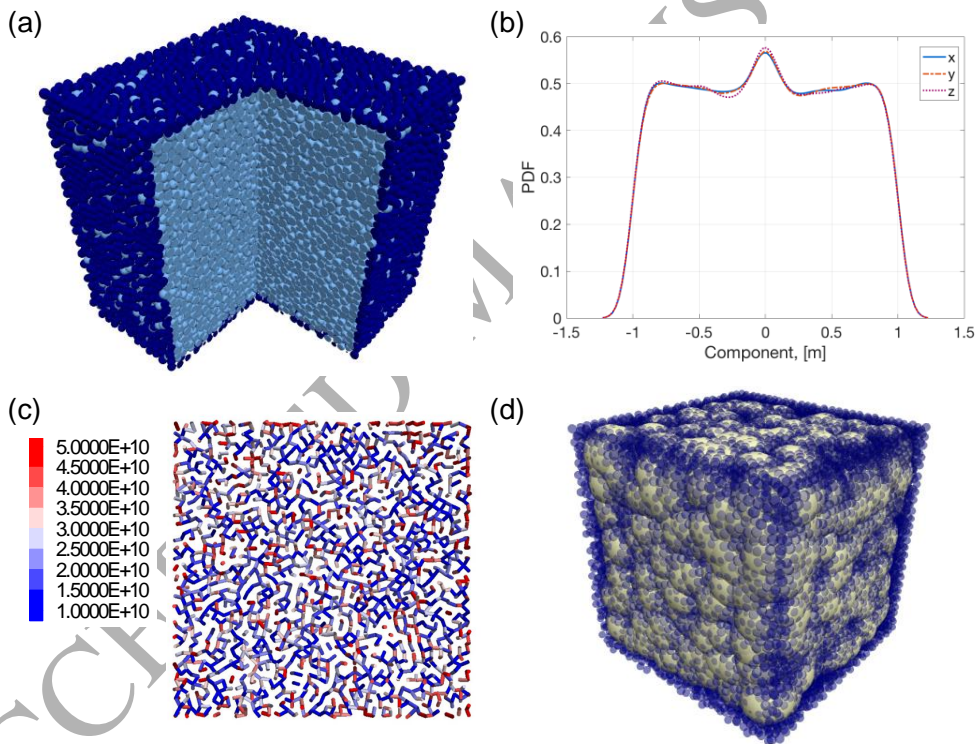

Figure 4: Properties of a typical modeled assembly: a) 3D representation, dark blue elements are the grip elements; b) probability distribution function of bond orientations; c) bonds as seen on a cross-section of the assembly colored by their anisotropic shear stiffnesses, [Pa/m]; d) measurement spheres.

4.2 Measuring Average Stresses and Strains in the Assembly

Stresses and strains in the assembly were computed using spherical measurement volumes (O'Sullivan, 2011; Potyondy and Cundall, 2004). Their radii and placement were random,

11

the former being user-defined and the latter being constrained to exist fully within the assembly. Specifically, stresses and strain rates were measured and strains were computed through time integration of the measured strain rates. Stresses and strain rates were averaged over all measurement spheres. A total of 5,000 measurement spheres were typically used, each with a radius that corresponds to 6 times mean element radius. On average, 165 elements contributed to the stress/strain measurement of each measurement sphere.

4.3 Determining the Size of the Minimum Representative Volume

The minimum representative volume (MRV) is the smallest assembly with a sufficient number of elements to produce an average macroscopic response independent of assembly size. The MRV is typically evaluated by the convergence of effective properties, in this case the averaged C_{11}, C_{12} and C_{44} constants of a cubic material. The MRV was determined as the next-to-smallest assembly size in which variation in properties from one assembly to another originated solely from uncertainty in the randomly placed measurement spheres rather than the variations in assembly packing. The MRV was found for an assembly with model parameters described in Section 4.1. The gap parameter was $0.17\,\bar{R}$ which corresponded to a stable element coordination number of $C_n \approx 8$. Tested assemblies had between 5,000 and 80,000 elements.

4.4 Computing the Stiffness Tensor

MRV assemblies were used for computing the full stiffness tensor. Element assemblies were deformed along the six independent strain paths (three uniaxial strain and three pure shear) up to a maximum strain of 10^{-3}. During each of these simulated deformations the assembly's internal stress and strain state was determined using measurement spheres as described previously.

Uniaxial compression simulations were performed by setting the grip element velocities to

$$\mathbf{u} = -\dot{\gamma}\begin{bmatrix} x_c & 0 & 0 \end{bmatrix} \tag{17}$$

$$\mathbf{u} = -\dot{\gamma}\begin{bmatrix} 0 & y_c & 0 \end{bmatrix} \tag{18}$$

$$\mathbf{u} = -\dot{\gamma}\begin{bmatrix} 0 & 0 & z_c \end{bmatrix} \tag{19}$$

for deformations label as $\boldsymbol{\varepsilon}^{(1)}, \boldsymbol{\varepsilon}^{(2)}, \boldsymbol{\varepsilon}^{(3)}$ deformations respectively. For the cases of pure shear deformation strains $\boldsymbol{\varepsilon}^{(4)}, \boldsymbol{\varepsilon}^{(5)}, \boldsymbol{\varepsilon}^{(6)}$ are imposed by grip element velocities of:

$$\mathbf{u} = \dot{\gamma}\begin{bmatrix} 0 & z_c & y_c \end{bmatrix} \tag{20}$$

$$\mathbf{u} = \dot{\gamma}\begin{bmatrix} z_c & 0 & x_c \end{bmatrix} \tag{21}$$

$$\mathbf{u} = \dot{\gamma}\begin{bmatrix} y_c & x_c & 0 \end{bmatrix} \tag{22}$$

12

with $\dot{\gamma} = 0.2$ 1/s. For each of the six deformations linear fits of stress/strain *vs.* time were performed to each of the six stress/strain components so that the ith and j^{th} components of stress and strain during the kth deformation are described by:

$$\sigma_i^{(k)} = a_i^{(k)} t \,, \tag{23}$$

$$\varepsilon_j^{(k)} = b_i^{(k)} t \,, \tag{24}$$

where the slopes *a* and *b* are fitting parameters. The stress and strain are related via the stiffness tensor giving six sets of six coupled equations:

$$\sigma_i^{(k)} = C_{ij} \varepsilon_j^{(k)} \,, \quad i, j, k = 1 \dots 6 \tag{25}$$

(36 equations in total), which can be written also in terms of the fitted slopes:

$$a_i^{(k)} = C_{ij} b_j^{(k)} \,, \quad i, j, k = 1 \dots 6 \tag{26}$$

The stiffness tensor must be symmetric about its diagonal ($C_{ij} = C_{ji}$) and so contains only 21 independent elements. To reduce the system to 21 independent equations, the equations for stress elements under conjugate deformation paths were added together to obtain equations:

$$a_i^{(k)} + a_k^{(i)} = C_{ij} b_j^{(k)} + C_{kj} b_j^{(i)}, \text{ for } i \le k \tag{27}$$

The motivation for this approach is to impose only the conditions on C_{ij} required to satisfy Newton's third law. If the assembly is truly behaving as a cubically anisotropic elastic medium, it should be evident from computing the full stiffness tensor. The systems of 21 coupled equations in (26–27) were solved numerically using the generalized minimal residual (GMRES) method in *MATLAB* (Saad and Schultz, 1986). The results were rounded to 0.1 GPa.

Stiffness tensor components obtained with DEM have a certain amount of statistical noise because they are obtained with a randomly distributed bond network. This introduces slight differences in the values of elastic constants that would be otherwise equal, and similarly gives small non-zero values when they must be zero for a continuum. Uncertainties were quantified as the largest deviation of each group of constants from the mean value of a symmetrized tensor. This included the average magnitude of small non-zero terms in the stiffness tensor that should be equal to zero.

By computing the 21 independent elements of the stiffness matrix explicitly, and demonstrating the correct rotational invariance of the properties, it was shown that the assemblies' properties possessed the correct cubic symmetry. Once this was established further calculations of elastic moduli were performed using a single deformation with simultaneous compression along *y* with shear applied in the *xz* plane. This deformation was imposed by assigning a velocity *u*

13

to the external grip elements based on their position relative to the center of the assembly, $\mathbf{x_c}=[x_c, y_c, z_c]$:

$$\mathbf{u} = \gamma \left[\begin{array}{ccc} z_c & \dfrac{y_c}{2} & x_c \end{array} \right] \tag{28}$$

where $\dot{\gamma}$ is the strain rate. Simulations were continued until the strains reached values between 1×10^{-5} and 1×10^{-3}.

4.5 Determining the Accessible Anisotropic Space

Parameter sweeps were used to determine the applicability of the proposed approach for modeling cubic materials. Parameter sweeps included changing values and ratios of the a_i and a_j constants (Eq. 9-15) as well as normal to shear stiffness ratios from Eq. 6-7. Simulations were performed for materials with $Z>1$ and $Z<1$. The limits of the anisotropic behavior were determined and results were compared with known values for common cubic materials (Simmons and Wang, 1971). Table 1 shows ranges of parameters used in the sweeps.

Table 1: Ranges of parameters used in determining the accessible anisotropic space.

Material	a_n	a_s	a_s/a_n	k_n	k_n/k_s
Z>1	0.01-5.0	0.01-100	0.01-500	1×10^{13}	1-5,000
Z<1	0.01-10.0	0.01-50	0.01-500	1×10^{13}	1-5,000

5 RESULTS

5.1 Minimum Representative Volume and Gap Cutoff Parameter

The *minimum representative volume* (MRV) was determined using a representative set of spheroid parameters for a material with a Zener ratio larger than one. Normal stiffness followed the 4 spheroid distribution with $a_n=4.31$ and $k_n=1 \times 10^{13}$ (Eq.6 and Eq.12-15) and shear stiffness the three spheroid distribution with $a_s=10.0$ and $k_s=3.55 \times 10^{12}$ (Eq.6 and Eq.9-11). The influence of the gap cutoff parameter on bonding and the elastic response was also quantified. The variation in elastic constants with the number of elements in an assembly is shown in Figure 5a and MRV was chosen to measure 30,700 elements. Also, the coordination number as a function of maximum gap size (Eq.4) is shown in Figure 5b.
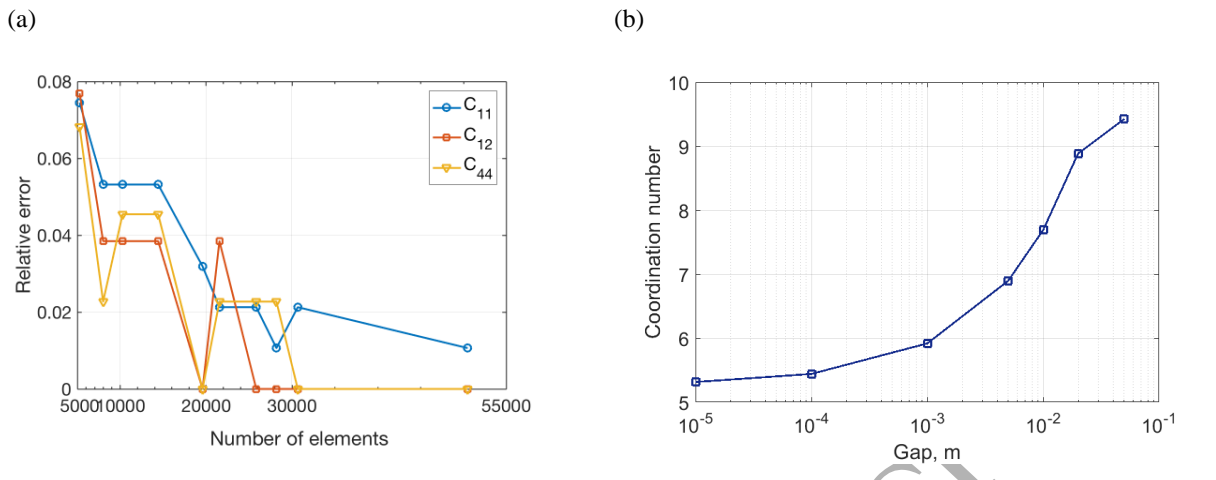
14

Figure 5: (a) Normalized elastic constants as a function of element number. MRV was chosen to have 30,700 elements. Values were normalized by those obtained with the largest assembly (82,238 elements) (b) Coordination number of a MRV assembly as a function of maximum gap parameter. Gap cutoff parameter was $0.17\bar{R}$ and yields a stable element coordination number of 7.7.

5.2 Description of the Model Assembly

The standard assembly used in subsequent simulations consisted of 30,700 elements held together with 118,008 bonds and an average coordination number of 7.7. This results in a cubic assembly with sides of length 60.0 $\bar{R}$. Figure 6 shows the elastically deformed assembly and Figure 7 shows an example elastic response of the assembly.
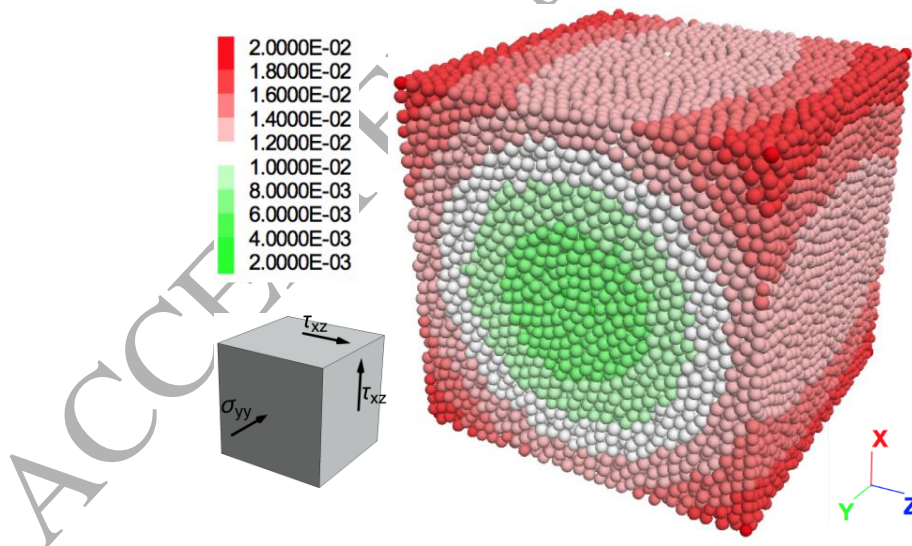

Figure 6: MRV assembly compressed in the y direction and sheared in xz. Elements are color-coded by the magnitude of element displacement in units of the mean element radius $\bar{R}$.

15

The stress-strain curves in Figure 7 generally follow a linear trend, except for a very small region at the beginning of the simulation. Final strains were at least two orders of magnitude larger in the directions of specified deformations relative to the unstrained directions.
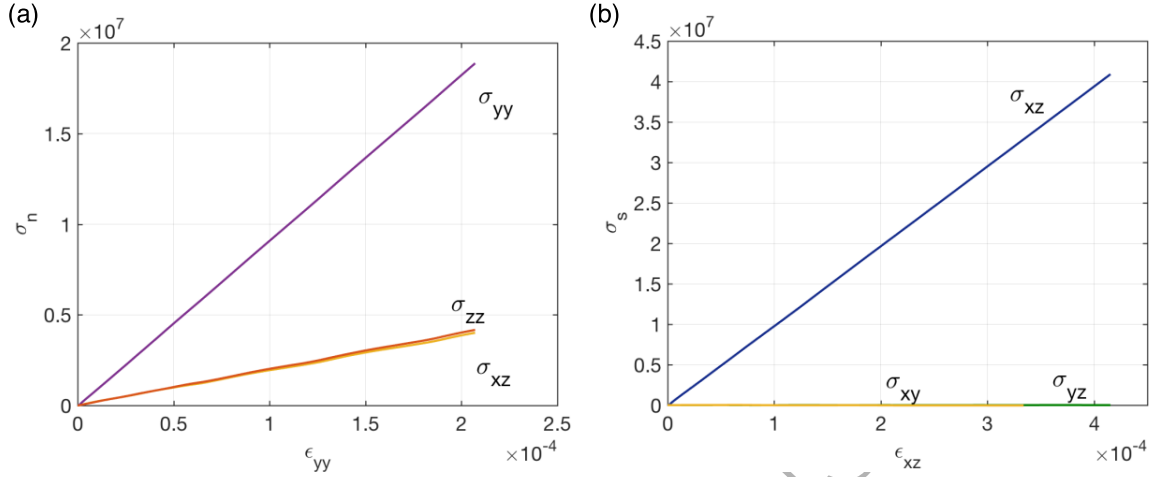

Figure 7: Stresses-strain curves in the deformation directions, (a) normal and (b) shear, and the corresponding elastic constants. Stress-strain curves are linear besides in the initial part of the simulation.

5.3 Full Stiffness Tensor

The full stiffness tensor was obtained for a representative case of anisotropy parameters, the same as the one used for the MRV. The full stiffness tensor the DEM assembly was measured to be:

$$C_{ij} = \begin{pmatrix} 75.5 & 30.4 & 30.4 & 0.05 & -0.3 & 0.4 \\ 30.4 & 76.3 & 30.9 & 0.2 & 0.05 & 0.2 \\ 30.4 & 30.9 & 76.1 & 0.2 & 0.05 & 0 \\ 0.05 & 0.2 & 0.2 & 28.7 & 0 & 0.05 \\ -0.3 & 0.05 & 0.05 & 0 & 28.5 & 0.05 \\ 0.4 & 0.2 & 0 & 0.05 & 0.05 & 28.6 \end{pmatrix} GPa \qquad (29)$$

Averaging the cubically equivalent so stiffness element, and setting to zero those that would be zero under cubic symmetry give the tensor:

$$C_{ij} = \begin{pmatrix} 76.0 & 30.6 & 30.6 & 0 & 0 & 0 \\ 30.6 & 76.0 & 30.6 & 0 & 0 & 0 \\ 30.6 & 30.6 & 76.0 & 0 & 0 & 0 \\ 0 & 0 & 0 & 28.6 & 0 & 0 \\ 0 & 0 & 0 & 0 & 28.6 & 0 \\ 0 & 0 & 0 & 0 & 0 & 28.6 \end{pmatrix} GPa. \tag{30}$$

Here $\bar{C}_{11} = \frac{(C_{11}+C_{22}+C_{33})}{3}$, $\bar{C}_{12} = \frac{(C_{12}+C_{13}+C_{23})}{3}$, and $\bar{C}_{44} = \frac{(C_{44}+C_{55}+C_{66})}{3}$. The variations in stiffness of the cubically equivalent element, including the ones that would be zero, provides a method for quantifying uncertainty. The largest uncertainty in this set of stiffness elements is in C_{11} and C_{12} values and measures 0.3 GPa. The C_{44} uncertainty is 0.1 GPa whereas the mean magnitude of terms that should otherwise be zero measures 0.15 GPa. These uncertainties are below detection in typical mechanical deformation experiments. The symmetry and cubic nature of the tensor presented in Eq.29-30 implies that to use the proposed approach only two deformations are needed to describe a cubic material in the model.

5.4 Rotational Invariance of the Stiffness Tensor

The same model discussed in Section 5.3 was used to assess the rotational invariance of the elastic properties. The rotation matrix applied to obtain the rotated stiffness tensor is presented in Eq.31:

$$\mathbf{R} = \begin{pmatrix} -0.3062 & -0.9186 & 0.2500 \\ 0.8839 & -0.1768 & 0.4330 \\ -0.3536 & 0.3536 & 0.8660 \end{pmatrix} \tag{31}$$

which corresponds to angles of 60°, 30°, and 45° about the x, y, and z axes, respectively. Rotating the stiffness tensor Eq.30 with this transformation matrix gives the tensor:

$$C_{ij} = \begin{pmatrix} 80.3 & 29.2 & 27.7 & 0.5 & -3.0 & 1.3 \\ 29.2 & 79.2 & 28.8 & 1.9 & 1.1 & -2.6 \\ 27.7 & 28.8 & 80.7 & -2.4 & 1.9 & 1.2 \\ 0.5 & 1.9 & -2.4 & 26.8 & 1.2 & 1.1 \\ -3.0 & 1.1 & 1.9 & 1.2 & 25.7 & 0.5 \\ 1.3 & -2.6 & 1.2 & 1.1 & 0.5 & 27.2 \end{pmatrix} GPa \tag{32}$$

This tensor represents the stiffness tensor if the principle axis of the stiffness distributions instead of being aligned with the Cartesian axis were rotated by $\boldsymbol{R}^{-1}$. We can therefore verify that the elastic behavior is rotationally invariant by assigning the stiffnesses to the assembly from the spheroid distributions rotated by $\boldsymbol{R}^{-1}$ and then computing the DEM stiffness tensor. The result is:

$$C_{ij} = \begin{pmatrix} 80.2 & 29.2 & 27.5 & 0.7 & -3.4 & 1.8 \\ 29.2 & 79.4 & 29.1 & 2.3 & 0.7 & -2.4 \\ 27.5 & 29.1 & 81.2 & -2.2 & 2.0 & 1.4 \\ 0.7 & 2.3 & -2.2 & 26.9 & 1.2 & 1.2 \\ -3.4 & 1.0 & 2.0 & 1.2 & 25.7 & 0.5 \\ 1.8 & -2.4 & 1.2 & 1.2 & 0.5 & 27.2 \end{pmatrix} GPa \tag{33}$$

which is in good agreement with Eq.32 within the uncertainty established from Eqs.29 and 30. Rotating Eq.33 back and diagonalizing as in case of full stiffness tensor (Eq.30) yields:

$$C_{ij} = \begin{pmatrix} 75.9 & 30.8 & 30.8 & 0 & 0 & 0 \\ 30.8 & 75.9 & 30.8 & 0 & 0 & 0 \\ 30.8 & 30.8 & 75.9 & 0 & 0 & 0 \\ 0 & 0 & 0 & 28.8 & 0 & 0 \\ 0 & 0 & 0 & 0 & 28.8 & 0 \\ 0 & 0 & 0 & 0 & 0 & 28.8 \end{pmatrix} GPa \tag{34}$$

with uncertainty in C_{11}, C_{12}, and C_{44} of 0.7, 0.7, and 0.1 GPa, respectively. The average value of the non-zero terms that should otherwise be zero is 0.2 GPa. The tensors in Eq.30 and Eq.34 agree to within 0.1, 0.2, and 0.2 GPa for C_{11}, C_{12}, and C_{44}, implying rotational invariance of the proposed anisotropy approach.

5.5 Reproducibility with Different Assemblies

To establish that the model's elastic behavior is robustly reproducible with different element assemblies the stiffness tensor calculations were repeated for two additional DEM samples generated with different random seeds. These different element assemblies had the same average packing density and a similar total number of elements, (30,714 and 30,718 compared to original 30,700). For all three assemblies, the elastic response was obtained using two different sets of model parameters that yielded the elastic constants of $C_{12}/C_{11}=0.3$ and $C_{44}/C_{11}=0.43$. Results are shown in Table 2. The elastic constants are very close for the three different assemblies in case of both parameter sets indicating that the model is reproducible and can be readily applied to various DEM assemblies.

Table 2: Elastic response of DEM assemblies generated with different random seeds.

PARAMETER SET	VALUE	SAMPLE 1	SAMPLE 2	SAMPLE 3
SET 1	C_{12}/C_{11}	0.30	0.30	0.31
	C_{44}/C_{11}	0.43	0.44	0.44

SET 2	C_{12}/C_{11}	0.30	0.30	0.31
	C_{44}/C_{11}	0.42	0.42	0.42

5.6 Accessible Anisotropic Space

In order to determine the space of cubic elastic anisotropy that can be accessed by the DEM model, simulations were performed to compute a random cloud of elastic moduli for model parameters selected with a uniform random sampling of the normalized log space. The resulting data cloud showing the anisotropic space accessible by both the Z<1 and Z>1 models is shown in Figure 8. For reference, this accessible space is plotted alongside the literature reported moduli for a wide range of cubic materials (Simmons and Wang, 1971). The domain of the elasticity space that can be accessed here is a property of the granular model and is not expanded by extending the range of the model parameters sampled.
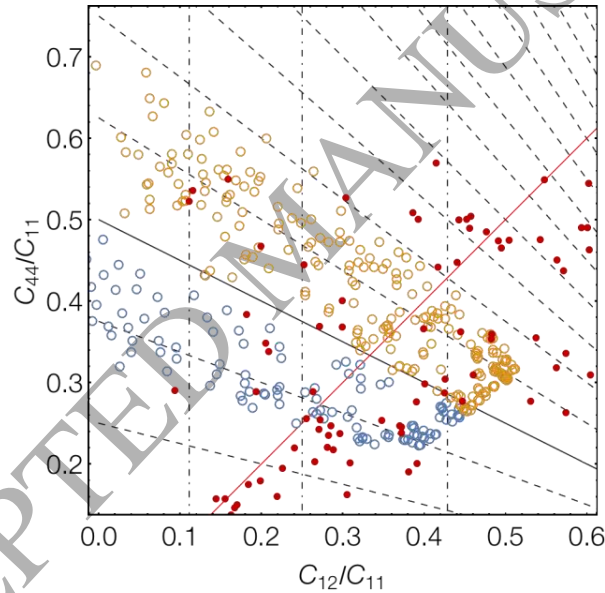

Figure 8: Comparison of elastic behavior with cubic materials. Red dots show literature reported elastic constants for a variety of cubic metals, ceramics, and oxides (Simmons and Wang, 1971). The open circles show the elastic moduli obtained with the DEM model from a random sampling of the α_n, α_s, and α_k normalized log space. In this plot, the vertical dot-dashed grid lines are contours of constant Poisson ratio in the ⟨100⟩ direction, $C_{12}/(C_{11}+C_{12})$ in steps of 0.1. The dashed black lines emanating radially from the bottom right are contours of constant Zener ratio (in steps of 0.25), with the solid line showing the contour for Zener ratio =1, and thus isotropic behavior. The red line cutting from bottom left to top right is the line along which the Cauchy symmetry relation, $C_{12}=C_{44}$, holds true.

5.7 Obtaining Specific Model Parameters

Because the space of model input parameters is three dimensional while the space of the resulting model's normalized elastic moduli is two dimensional, many different model
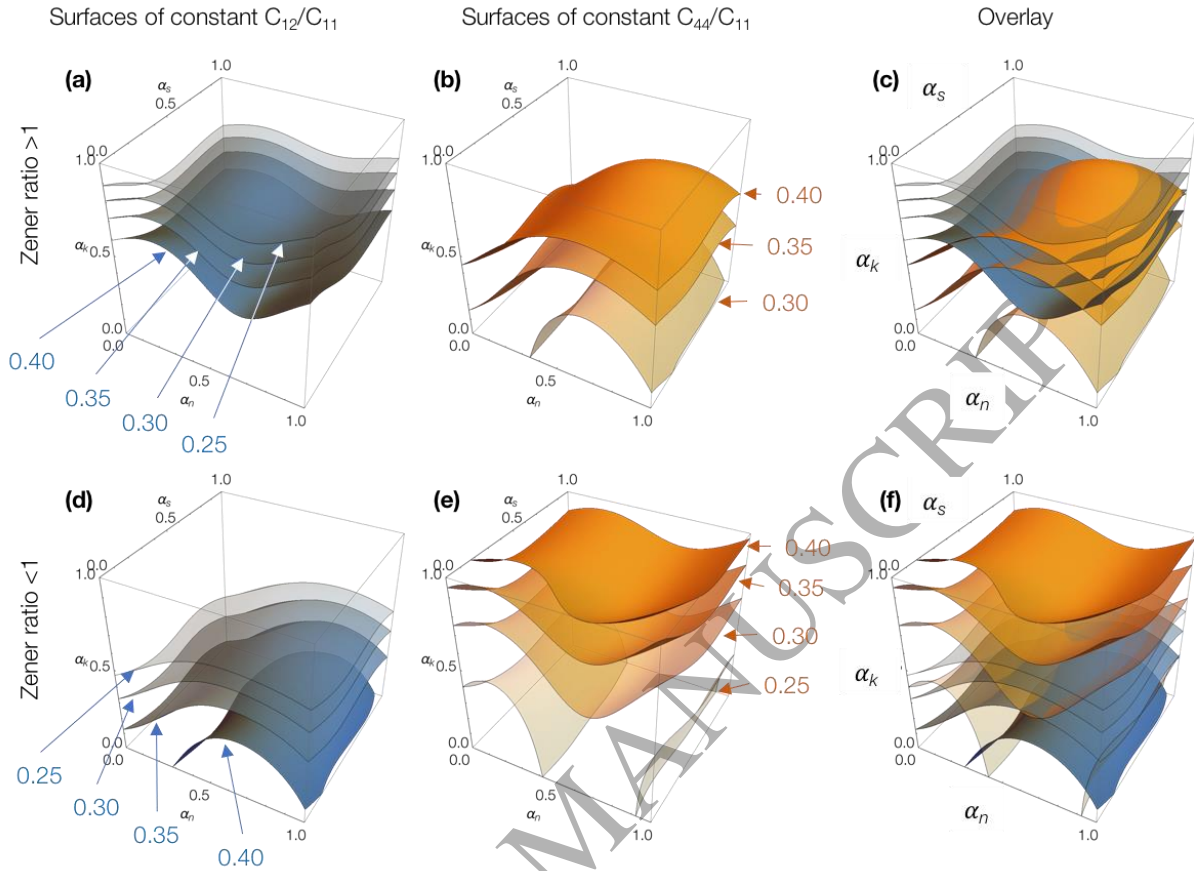
Figure 9: Surfaces of constant elastic moduli plotted in the space of log-normalized model parameters with the x,y, and z axes the normal, shear, and stiffness ratios respectively. Blue surfaces (plots (a) and (d)) are contours of C_{12}/C_{11} ratio. Orange surfaces (plots (b) and (e)) are contours of C_{44}/C_{11}. The top row (plots (a–c)) are for the Zener ratio >1 model, while the bottom row is for the Zener ratio < 1 model. Plots (c) and (f) show the two moduli contours overlaid.

parameters sets can lead to the same anisotropic elastic behavior. To elucidate the mapping from model parameters to emergent elastic moduli (and to enable efficient determination of model parameters for a desired elasticity) interpolation schemes have been developed based on an artificial neural network (ANN). Feed forward ANNs with a two hidden layers of nine neurons each were trained to a randomly selected set of 70% of the log normalized model parameters used to compute moduli plotted in Figure 9. For both the Z<1 and the Z>1 models twenty ANNs were trained starting from different initial conditions, and the variance between the ANNs used to test the quality of training and uncertainty in the interpolation. The trained ANNs reproduced a validation dataset (half of the remaining data selected at random) with an R-squared value better than 0.997 — as well as should be expected for the uncertainty in the computed elastic moduli. Using these ANN to explore the model parameter space in Figures 9 & 10 shows contour surfaces in the log-normalized parameter space that have constant elastic moduli — Figure 9 shows isosurfaces of dimensionless C12 and C44, while Figure 10 shows isosurfaces of Zener ratio and constant Poisson ratio along $\langle 100 \rangle$, defined as $C_{12}/(C_{11}+C_{12})$. These plots show that for

any desired elastic response there are a range of possible model parameters that could reproduce it. The question of which alternative a user should choose will be discussed in more detail.
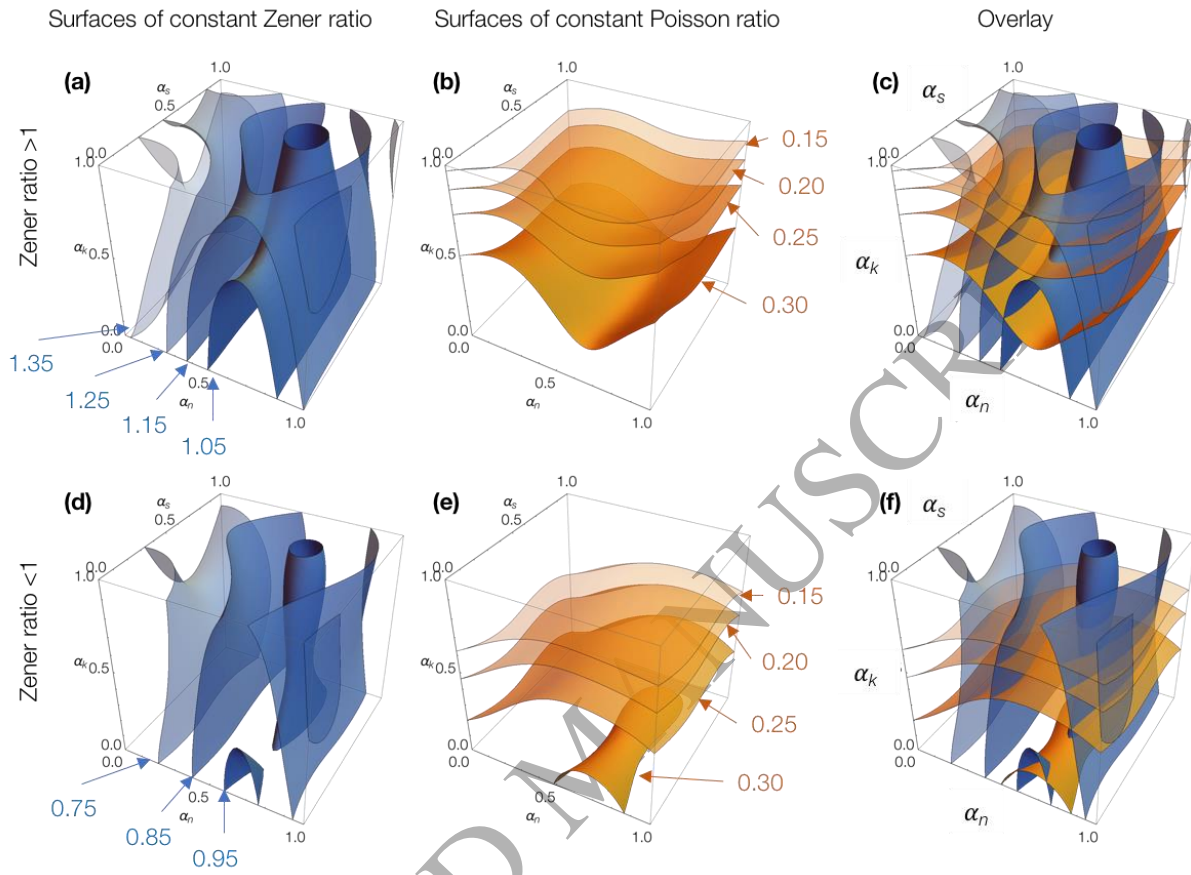

Figure 10: Surfaces of constant Poisson ratio plotted in the space of log-normalized model parameters with the x,y, and z axes the normal, shear, and stiffness ratios respectively. Blue surfaces (plots (a) and (d)) are contours of constant Zener ratio $2C_{44}/(C_{11}-C_{12})$ ratio. Orange surfaces (plots (b) and (e)) are contours of constant $\langle 100 \rangle$ Poisson ratio defined as $C_{12}/(C_{11}+C_{12})$. The top row (plots (a–c)) are for the Zener ratio >1 model, while the bottom row is for the Zener ratio < 1 model. Plots (c) and (f) show the two moduli contours overlaid.

6 DISCUSSION

6.1 Limits of the Accessible Domain of Elastic Properties

It is clear from the data cloud plotted in Figure 8 that there is only a limited domain of the elasticity space that can be accessed by the DEM models, and there are many known cubic materials possessing elastic constants that fall outside this domain. It is thus worthwhile to consider what sets the fundamental limits of the DEM model, and what this tells us more generally about the nature of atomic bonding. The domain of accessible moduli can be roughly described as having Zener ratios between 0.65 and 1.5 with $C_{44} > 0.6\ C_{12}$. The surfaces of constant modulus in Figures 9 show that in both the Zener ratio >1 and the Zener ratio < 1 models the strongest influence on elastic properties is the change in the ratio of shear to normal stiffness, a_k, with C_{12} diminishing and C_{44} increasing as a_k is increased. In the Zener ratio <1 model the isosurfaces for C_{12} (C_{44}) are concave up (down) with varying anisotropy of the normal stiffness distribution. These surfaces have a valley in the log normalized parameter space running along $\alpha_n \approx 0.7$. This corresponds to a normal stiffness anisotropy ratio of $a_n = 1$, the condition of no directional dependence in bonds' normal stiffness. In the Zener ratio >1 model the directions of curvature of the C_{12} and C_{44} isosurfaces are reversed. The parameter that has the weakest impact on the models' elastic moduli is α_s, the anisotropy ratio of the shear stiffness, which is perhaps not surprising as the input parameter space was restricted so that shear stiffness amplitudes were always softer that normal stiffnesses.

Rather than considering the normalized C_{12} and C_{44} moduli it is instructive to examine surfaces of constant Zener ratio and $\langle 100 \rangle$ Poisson ratio ν (the ratio of lateral contraction due to an elongation along a $\langle 100 \rangle$ direction and defined by $C_{12}/(C_{11}+C_{12})$) as is shown in Figure 10. The Poisson ratio is similar in behavior to C_{12} in Figure 9, being strongly dependent on a_k. The Poisson ratio increases quickly with diminishing shear stiffness when the stiffness ratio is just less than 1, but the speed of change slows once the shear stiffness is negligible in comparison to the normal stiffness. When the stiffness ratio is just less than 1 the DEM assemblies exhibit ν close to zero (that is, there is no coupling between deformations in orthogonal directions), and for shear stiffnesses larger than the normal stiffnesses the DEM assemblies become auxetic. This
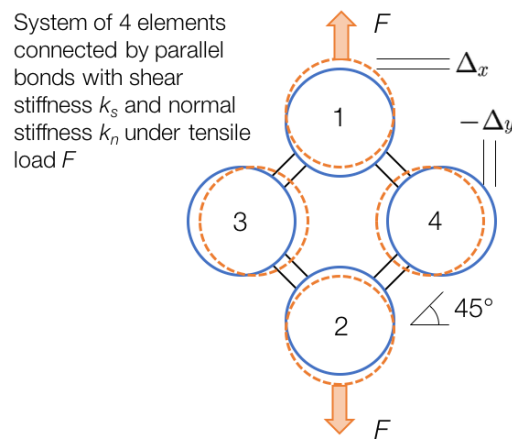

Figure 11: Idealized 4 element model to illustrate the effect of normal to shear stiffness ratio on the Poisson contraction.

2

unusual behavior can be understood by considering the deformation of an idealized case of four identical elements connected by parallel bonds at 45° to a loading axis (see Figure 11). It is trivial to show that the Poisson ratio of this idealized element cluster is

$$\nu = \frac{-\Delta_y}{\Delta_x} = \frac{k_n - k_s}{k_n + k_s} \tag{35}$$

Clearly if this simple model were rotated by 45° so that the bonds were parallel or perpendicular to the loading the Poisson contraction of the assembly would be zero, and so with a large random assembly the collective behavior will fall between these extremes.

The simple example in Figure 11 shows that Poisson contraction of the DEM assembly originates from the balance of shear and normal deformations of the bonds. The contraction does not originate from geometric rotation of bonds acting like network of pinned bars in a complex truss — a good thing as the atomic bonding in a material are not simple pair interactions. However, the Poisson contraction is still a collective property and does not stem from Poisson contraction of individual elements. Each element represents a chunk of elastic material seamlessly welded to its neighbouring elements, and so each element should experience a Poisson contraction. This is not captured in standard DEM models which treat elements as rigid and represent their elastic behavior with independent contact laws. Correctly capturing Poisson coupling in this formalism would require the equilibrium length of a bond between two elements to alter based on the combined state of all the other bonds those elements participate in. This is a fundamental limitation of the current parallel bond DEM that we will seek to remedy in future work, and unfortunately, may require losing the simplicity of independent local contact laws. It is clear from Figures 8–10 that the DEM networks simulated in this work have trouble producing a Poisson ratio greater than about 0.3. It was found that this limit could be increased by changing the density of the bonding network to reduce the average element coordination, but a thorough investigation of this is beyond the scope of this manuscript.

Also shown in Figure 10 are surfaces in parameter space with constant Zener ratio. It can be seen that these lie vertically and so are only weakly coupled to the stiffness ratio, a_k. The anisotropy increases as a_n or a_s move away from 1 (α_n or α_s move away from 0.703), and dependence on a_s fades as a_k diminishes. The limit to the elastic anisotropy achievable with the DEM model can be understood by looking at the plots of the directionally dependent stiffness shown in Figure 3 (and also later in Figure 12). As the shear or normal anisotropy parameter becomes large or small the corresponding stiffness distribution becomes very acute, either composed on needle like lobes or pancake like discs. In these extreme cases, the solid angle subtended by the directions of high stiffness is very low and, as the elements have an average coordination of eight, the likelihood of a contact lying exactly along the stiff direction becomes low. This means that although the bond stiffnesses are highly anisotropic, there are a number of very stiff bonds embedded in a network of much softer bonds and thus one would expect to require a large MRV.

Beyond the problem of numerically sampling a stiffness distribution with long tails, a second and more fundamental limit on the accessible elastic properties is set by the integral of the stiffness

functions. In Appendix C, the analytic model derived in Appendix A is compared with the DEM simulations. Performing a random sampling of the parameter space, as was performed for DEM in Figure 8, produces a very similar accessible domain of elasticity as that shown in Figure A.1. The analytic model and DEM simulations display elastic anisotropy ranging from 0.6 to 1.5. Where the models differ is in their ability to cross the red $C_{12}=C_{44}$ line.

In Appendix D, the analytic model is used to determine how the limits of the accessible elastic domain are related to the angular stiffness functions. For expanding this domain to reach more extreme anisotropies, it is shown that larger values of Z can be achieved if the stiffness functions are altered to permit independent tuning of shear and normal stiffness along the $\langle 110 \rangle$ directions. To test this a set of modified stiffness functions was defined that added or subtracted a stiffness contribution due to a function defined as the envelope of six spheroids aligned along $\langle 110 \rangle$. For the $Z>1$ model these new stiffness functions were defined with the normal stiffness $k_n(\boldsymbol{n}, a_n) = k_o\left(r_{\langle 111 \rangle}(\boldsymbol{n}, a_n) + 0.5 r_{\langle 110 \rangle}(\boldsymbol{n}, a_n)\right)$, and shear stiffness $k_s(\boldsymbol{n}, a_s) = k_o\left(r_{\langle 100 \rangle}(\boldsymbol{n}, a_s) - 0.5 r_{\langle 110 \rangle}(\boldsymbol{n}, a_s)\right)$, where $r_{\langle 100 \rangle}$, $r_{\langle 111 \rangle}$, and $r_{\langle 110 \rangle}$ are radial functions describing the envelope of three, four, and six overlapping spheroids aligned with the principal axes along the $\langle 100 \rangle$, $\langle 111 \rangle$, and $\langle 110 \rangle$ directions, respectively. For the $Z<1$ model the stiffness functions were $k_n(\boldsymbol{n}, a_n) = k_o\left(r_{\langle 100 \rangle}(\boldsymbol{n}, a_n) + 0.5 r_{\langle 110 \rangle}(\boldsymbol{n}, a_n)\right)$, and $k_s(\boldsymbol{n}, a_s) = k_o\left(r_{\langle 111 \rangle}(\boldsymbol{n}, a_s) - 0.5 r_{\langle 110 \rangle}(\boldsymbol{n}, a_s)\right)$. The domain of elasticity that can be accessed using these functions is also plotted in Figure A.1(a) and is considerably wider in Z that the simpler model, but is still bounded by the $C_{12}=C_{44}$ line.

To examine the cause of the $C_{12}=C_{44}$ boundary, Appendix D also examines the integral that dictates the quantity $C_{12} - C_{44}$. This was found to be always negative; there is no modification that could make this positive. That is, a system of parallel bonds deformed homogeneously cannot have $C_{12} - C_{44} > 0$. This then raises a question: what is different about the DEM simulations that enables $C_{12} - C_{44}$ to be positive in some circumstances? In the analytic model, it is seen that $C_{12} - C_{44}$ becomes identically zero when the shear stiffness goes to zero in agreement with the Cauchy relationship that $C_{12} = C_{44}$ in materials held together with center to center pair interactions only. That the DEM simulations are able break through this we attribute to non-homogeneous displacement of the elements. In the DEM simulations the orientation and stiffness of bonds is random, and thus the deformation field of the elements will include locally non-affine displacements. The result will be a larger fraction of elastic energy stored in bonds oriented in soft directions and deformation fields that could involve local rotation of clusters of elements. The authors speculate that these could be responsible positive values of $C_{12} - C_{44}$.

A more systematic approach to expanding the accessible elastic domain would be through the use of stiffness functions constructed from a more complete basis set. For example, one could define a stiffness distribution using a correctly symmetrized set of spherical harmonics. For more flexibility still, one could define the shear stiffness to depend on the direction of displacement in addition to the orientation of the bond. The standard parallel bond model used in DEM has only a single shear stiffness; that is, for a given contact normal, the shear stiffness is the same in all

directions perpendicular to the contact. This is not the case in a cubically elastic medium where, as can be seen in Figure 2, on any contact plane there will be a soft and stiff direction of shear.

6.2 Selection of Element Packing Density, Coordination, and Polydispersity

The choice of assembly packing fraction, element polydispersity, and coordination number all affect the collective macroscopic elastic behavior, but were not fully explored in this work. Rather, a set of reasonable choices for these parameters were found for which the sensitivity of the model to the variation in packing, element size distribution and element coordination was low.

The packing efficiency is quantified here by the assembly porosity, or *void fraction*, as is common in the geotechnical literature for granular materials. A lower limit of an admissible void fraction is 0.36 which corresponds to a closest possible packing of monodispersed spheres. Smaller void fractions can be obtained in highly polydisperse assemblies, but in this work the element size distribution was relatively low — only large enough to prevent regular crystal-like packing of elements. An upper limit of void fraction occurs at around 0.44 with the jamming transition in a non-bonded assembly, above which the assemblies become so loose that they are mechanically unstable. Although the elements in the assemblies in this work are bonded, the bonding network with a high void fraction would be very loose and thus a poor representation of an elastic continuum. The interaction cutoff for bonding adjacent elements was tuned so that the average element coordination was 8.0. In general, a higher coordination number may give macroscopic response closer to continuum behavior; however, more redundant bonding in and assembly inhibits Poisson contraction and so a compromise was needed reach higher Poisson ratios and C_{12} values relative to C_{11} and C_{44}.

6.3 Choosing Optimal Model Parameters

The most surprising result from Figure 10 is that it does not matter how one chooses to introduce anisotropy into the directional dependence of the bond stiffnesses. One can create a DEM model with the same macroscopic Zener anisotropy ratio using stiffness distributions defined by either oblate ($a < 1$) or prolate ($a > 1$) spheroids, providing one imposes the correct cubic symmetry of these distributions.[**] The concept is particularly noticeable in Figure 12 which shows the locus of parameters that all yield a particular elasticity tensor, along with spherical plots of the stiffness distributions that produced them. The contours show a remarkable mirror symmetry in the $a_s = 1$ plane ($\alpha_s = 0.703$ plane). For both the Zener ratio <1 and >1 models the angular functions for normal stiffness that produce the left-hand contour are built from prolate spheroids. These distributions resemble the angularly dependent normal stiffness in Figure 2, while the right-hand

---

[**]The authors speculate that this hints at a profound hidden symmetry in the way macroscopic elasticity emerges from collective microscopic interactions, but at this juncture the authors are uncertain of what this might be.

contour is constructed using oblate distributions of normal stiffness that appear to have little in common with the moduli in Figure 2.

At this point, some questions arise. Which of the many choices of parameters for a desired elastic response should one choose? And, how can one discriminate between the choices? and should one switch from angular functions based on spheroids to a basis set that provides more flexibility such as spherical harmonics?

Sticking with spheroid angular functions, a number of arguments can be made to steer the choice of model parameters. One approach is to choose parameters that reflect the underlying behavior of the material of interest. With this rationale, one might choose parameters in which the same anisotropy ratio is used for shear stiffnesses as for normal stiffness — restricting oneself to parameters on the diagonal $a_n = a_s$ plane as plotted in Figure 13. On this equianisotropy plane one still has to decide whether to use oblate ($a < 1$) or prolate ($a > 1$) distributions. Keeping with the philosophy of mimicking the bonding behavior of the material the best choice might be to use parameters with $a > 1$.

An alternative approach to choosing between model parameters that produce equivalent macroscopic elastic response is to ask what is different about the system at the microscopic level, and to choose the system with the least microscopic heterogeneity, and thus, the smallest MRV. With this rationale, one would choose the parameters for a_n and a_s closest to one – and when faced with the choice of prolate or oblate distributions, opting for oblate distributions would be preferable as these have a more equitable distribution of stiffness over a given solid angle. To quantify heterogeneity, we compute the mean normalized standard deviation of the distribution of local strains obtained from the set of measurement spheres. This noise metric for the eight sets of model parameters (labeled i–viii) along the contour in Figure 12(a) are given in Table 3. For this system which, is not strongly anisotropic, the distribution of local strains is narrow with a width of around 5-6%, for both the normal and shear components of strain. There is no obvious trend in this heterogeneity with the model parameters, other than that the noise in the normal strain is slightly larger than the noise in the shear strain.

An alternative means to quantify this internal state of the DEM assembly can be made indirectly by comparing the elastic moduli of the DEM element assembly to the moduli of the analytic model with the same stiffness functions. This comparison was also performed for parameter sets indicated in Figure 12(a) with the results reported in Table 3. In these cases the mean field analytic model and the DEM simulations are in good agreement and there is no overall trend in the deviation. The comparison was also performed over the entire log normalized parameter domain for the $Z > 1$ model as shown in Figure C.1(b) in Appendix C. Here the assumption is that differences between the mean field analytic model and the DEM model arise because of heterogeneous deformation and therefore, the deviation in moduli between the two is a metric of the heterogeneity in the DEM assembly. In Figure C.1(b) it can be seen that the deviation from mean field behavior depends most strongly on the ratio of the shear to normal stiffness, and that C_{12} matches the mean field model when the normal and shear stiffnesses have similar magnitudes, while C_{44} matches the mean field model when the shear stiffness is low.

26

As a final comment, the rationale for selecting the parameters for spheroid based models can be applied to choosing other angular functions and selecting the model parameters for these alternative functions. The advantage to be gained from selecting more flexible angular functions, besides reducing the MRV, is expanding the boundaries of accessible elastic behavior.
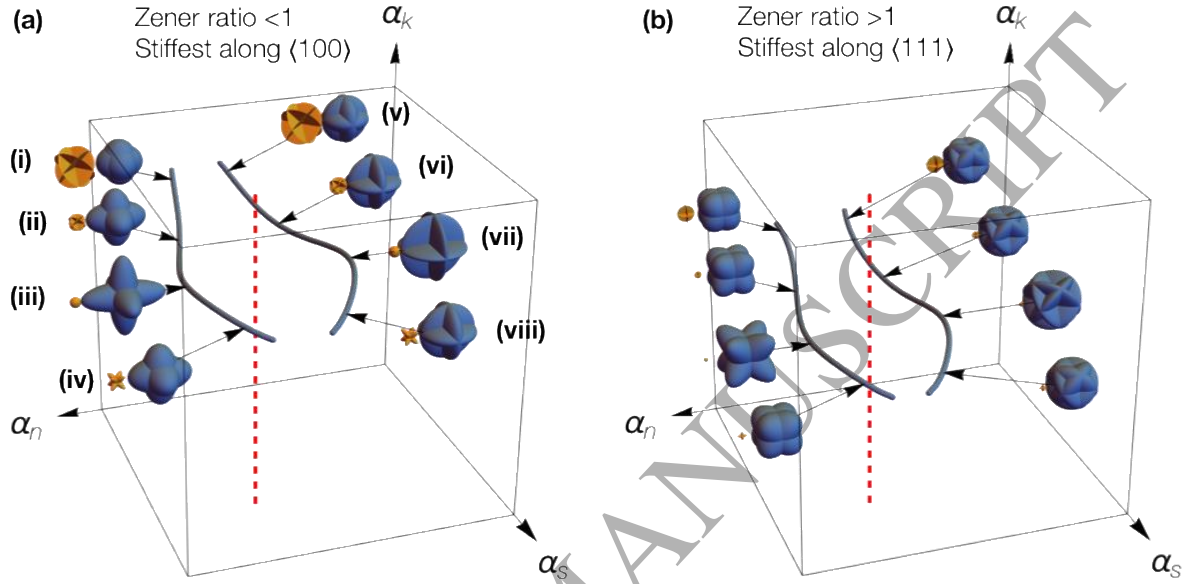

Figure 12: Contours of identical elastic behavior. Plot (a) shows contours of $C_{12}/C_{11}= 0.2$, and $C_{44}/C_{11}= 0.35$ for the Zener ratio <1 model. Plot (b) shows contours of $C_{12}/C_{11}= 0.35$, and $C_{44}/C_{11}= 0.35$ for the Zener ratio >1 model. The vertical dashed red line indicates the line along which the bond normal and shear stiffnesses are isotropic. The inset polar plots show the shear (gold) and normal (blue) stiffness distributions (all plotted on the same absolute scale).

Table 3: Table quantifying variation in internals state for DEM parameters shown in Figure 12.(a) which all have the same normalized elastic moduli of $C_{12}/C_{11} = 0.2$ and $C_{44}/C_{11} = 0.35$. The 2nd and 3rd columns show the mean normalized noise in measurement sphere normal and shear strains, and the last two columns quantify the deviation from the analytic model derived in Appendix A.

Model Parameters			Normalized measurement sphere noise (%)		Deviation from analytic model: $(C_{ij}/C_{11})_{DEM} - (C_{ij}/C_{11})_{Model}$	
Set	a_n	a_s	a_k	ε_1 (%)	ε_4 (%)	Deviation: Δ_{12}	Deviation: Δ_{44}
i	1.30	0.03	0.33	5.8	5.0	-0.028	0.017
ii	1.82	0.12	0.22	5.7	4.8	-0.013	0.003
iii	2.83	0.88	0.24	6.1	4.3	-0.008	-0.015

27

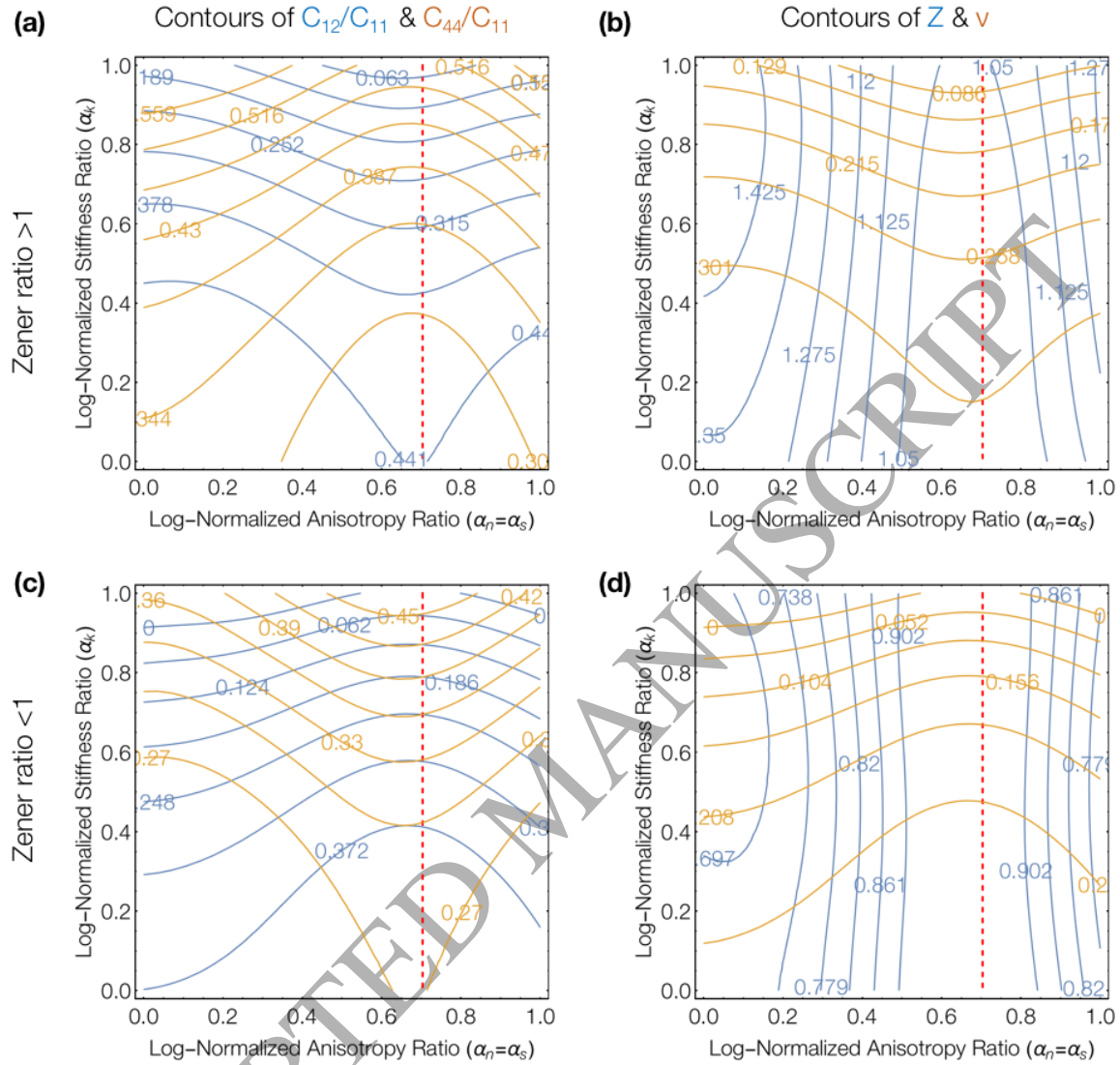| iv | 1.78 | 3.61 | 0.22 | 5.4 | 4.3 | -0.014 | 0.006 |
v	0.50	0.03	0.34	5.8	5.1	-0.025	0.014
vi	0.34	0.12	0.23	5.5	5.0	-0.012	0.006
vii	0.21	0.88	0.27	5.8	4.5	-0.007	-0.002
viii	0.38	3.61	0.22	5.4	4.5	-0.005	0.009

Figure 13: Contours of elastic moduli on the plane of the parameter space on which the normal and shear stiffnesses have identical anisotropy ratio ($\alpha_n=\alpha_s$). The red dashed line marks the parameters at which the normal and shear stiffnesses are isotropic ($a_n=a_s=1$). Plots (a & b) are for the Zener ratio >1 model and (c & d) are for Zener ratio <1. Plots (a & c) show the normalized moduli C_{12}/C_{11} (blue) and C_{44}/C_{11} (gold). Plots (b & d) show the Zener ratio (blue) and Poisson ratio (gold).

7   CONCLUSIONS

In this work, the discrete element method (DEM) was adapted to enable a random packing of elements to model materials with cubic anisotropy. The ability to capture cubic elasticity is a prerequisite for extending the discrete element method to model stochastic mechanical processes in monolithic solids which consist of cubically anisotropic elastic constituents (polycrystals, composites, etc.). Additionally, the DEM model presented here provides a roadmap for adapting traditional DEM to model orthotropic rocks and geotechnical materials. This extension to DEM

was accomplished using the established parallel bond contact formalism and is capable of modeling a broad range of cubic materials with Zener ratios smaller and larger than one. Anisotropy in the collective elastic response of the DEM assembly comes from assigning the stiffness of element to element bonds depending on the bonds' initial orientation — and crucially, assigning them using an angular dependence function that has the same underlying cubic symmetry as the crystal it mimics. In this first demonstrative work, these angular functions where defined by the envelope of three or four overlaid spheroids with principal axes aligned, respectively, along the ⟨100⟩ or ⟨111⟩ directions of the crystal being represented. The models have three parameters that define the overall elastic behavior (a_n, a_s, and a_k, respectively, the normal and shear stiffness anisotropy, and the ratio of the shear to normal stiffness magnitude). A fourth parameter sets the overall magnitude of the resulting stiffness tensor. Two different models were presented to capture the properties of materials with Zener ratio <1 and Zener ratio >1. It was demonstrated that the models' elastic behaviors have the correct symmetry and rotational invariance.

The research presented here also explored the mapping between the model parameters and the resulting elastic properties, and examined the limits on domain of elastic properties that can be accessed with the DEM model. An artificial neural network (ANN) was trained to interpolate between input DEM model parameters and the ensuing elastic moduli of the DEM assembly. The interpolation scheme enabled connections between the model parameters and resulting behavior to be elucidated efficiently and revealed the surprising result that only the scale of the asymmetry aspect ratio in the contact mechanics is important, not its direction of deviation. The ANN analysis further revealed that the input parameters are non-unique and thus a desired set of elastic stiffness tensor ratios can be achieved with numerous combinations of input parameters. Accompanying the DEM model, an analytic mean field model of the DEM elasticity was presented and used to examine the limit on the accessible domain of elastic properties. This model reveals that the accessible domain can be expanded to larger and smaller Zener anisotropy ratios by changing the functional form of the angular stiffness functions, but that there is a hard limit to increasing the Poisson ratio that is set by the Cauchy $C_{12}=C_{44}$ limit. The combination of the ANN and the mean field model can be used to quickly and efficiently choose an optimal set of DEM model parameters to represent a system with a specific desired stiffness tensor.

8 ACKNOWLEDGMENTS

APPENDIX A. ANALYTIC MODEL OF ELASTICITY

Consider a DEM assembly that contains N_b parallel bonds per unit length, uniformly distributed over orientation, and with an average length l. The bonds have normal and shear stiffness that

depend on orientation, $k_n(\hat{n})$, and $k_s(\hat{n})$ respectively. If the assembly is deformed with a homogeneous strain ε (and one assumes that deformation of the bonds is affine) then the displacement of a bond with orientation $\hat{n}$ is given by:

$$\mathbf{u} = l(\hat{n} \cdot \varepsilon) \tag{.36}$$

Where the displacement can be separated into normal and shear components:

$$u_n = \mathbf{u} \cdot \hat{n} = l(\hat{n} \cdot \varepsilon) \cdot \hat{n} \tag{.37}$$

and

$$u_s = |\mathbf{u} - u_n \hat{n}| = l\sqrt{(\hat{n} \cdot \varepsilon) \cdot (\hat{n} \cdot \varepsilon) - \hat{n}((\hat{n} \cdot \varepsilon) \cdot \hat{n})} \tag{.38}$$

The elastic energy stored in the deformed bond is:

$$\begin{aligned}
E_b(\hat{n}) &= \frac{1}{2} k_n(\hat{n}) u_n^2 + \frac{1}{2} k_s(\hat{n}) u_s^2 \\
&= \frac{1}{2} l^2 \left(k_n(\hat{n}) - k_s(\hat{n}) \right) \left((\hat{n} \cdot \varepsilon) \cdot \hat{n} \right)^2 + \frac{1}{2} l^2 k_s(\hat{n}) (\hat{n} \cdot \varepsilon) \cdot (\hat{n} \cdot \varepsilon)
\end{aligned} \tag{.39}$$

Averaging over all orientations gives the total elastic energy density:

$$E_v = \frac{N_b}{4\pi} \int d\hat{n} E_b(\hat{n}) \tag{.40}$$

The elements of the elastic stiffness tensor C_{ijkl} are given by the second derivative of the elastic energy density so that:

$$C_{ijkl} = d_{ijkl} \frac{\partial^2 E_v}{\partial \varepsilon_{ij} \partial \varepsilon_{kl}} \tag{.41}$$

where d_{ijkl} is the multiplicity of the symmetry equivalent index combinations (so that for example $d_{1111} = 1$, $d_{1122} = 2$, $d_{1112} = 4$, $d_{2323} = 4$, and $d_{2313} = 8$).

Switching to the notation of the reduced stiffness matrix, we can compute the stiffness element C_{ij} by imposing a homogeneous strain state $\varepsilon = \eta_i \varepsilon^{(i)} + \eta_j \varepsilon^{(j)}$: the sum of two superimposed strains with magnitudes η_i and η_j along strain directions $\varepsilon^{(i)}$ and $\varepsilon^{(j)}$. The energy density of the assembly with this deformation is:

$$E_v = \frac{N_b l^2}{8\pi} \int d\hat{n} \Big[(k_n - k_s)(\hat{n} \cdot \varepsilon \cdot \hat{n})^2 + k_s(\hat{n} \cdot \varepsilon) \cdot (\hat{n} \cdot \varepsilon) \Big]$$

$$= \frac{N_b l^2}{8\pi} \int d\hat{n} \begin{bmatrix} (k_n - k_s)\begin{pmatrix} \eta_i^2 (\hat{n} \cdot \varepsilon^{(i)} \cdot \hat{n})^2 + 2\eta_i \eta_j (\hat{n} \cdot \varepsilon^{(i)} \cdot \hat{n})(\hat{n} \cdot \varepsilon^{(j)} \cdot \hat{n}) \\ +\eta_j^2 (\hat{n} \cdot \varepsilon^{(j)} \cdot \hat{n})^2 \end{pmatrix} \\ +k_s \begin{pmatrix} \eta_i^2 (\hat{n} \cdot \varepsilon^{(i)}) \cdot (\hat{n} \cdot \varepsilon^{(i)}) + 2\eta_i \eta_j (\hat{n} \cdot \varepsilon^{(i)}) \cdot (\hat{n} \cdot \varepsilon^{(j)}) \\ +\eta_j^2 (\hat{n} \cdot \varepsilon^{(j)}) \cdot (\hat{n} \cdot \varepsilon^{(j)}) \end{pmatrix} \end{bmatrix} \quad .42$$

Taking the second derivatives with respect to η gives:

$$C_{ii} = d_{ii} \frac{\partial^2 E_v}{\partial \eta_i^2} = \frac{N_b l^2}{8\pi} \int d\hat{n} \Big[(k_n - k_s)(\hat{n} \cdot \varepsilon^{(i)} \cdot \hat{n})^2 + k_s(\hat{n} \cdot \varepsilon^{(i)}) \cdot (\hat{n} \cdot \varepsilon^{(i)}) \Big] \quad .43$$

$$C_{ij} = d_{ij} \frac{\partial^2 E_v}{\partial \eta_i \partial \eta_j}$$
$$= \frac{N_b l^2}{8\pi} \int d\hat{n} \Big[(k_n - k_s) 2 (\hat{n} \cdot \varepsilon^{(i)} \cdot \hat{n})(\hat{n} \cdot \varepsilon^{(j)} \cdot \hat{n}) + k_s 2 (\hat{n} \cdot \varepsilon^{(i)}) \cdot (\hat{n} \cdot \varepsilon^{(j)}) \Big] \quad .44$$

APPENDIX B. PROOF OF CUBIC ELASTICITY FROM SPHEROID STIFFNESS DISTRIBUTIONS

Cubic elasticity requires that $C_{11} = C_{22} = C_{33} \neq 0$, $C_{12} = C_{21} = C_{13} = C_{31} = C_{23} = C_{32} \neq 0$, $C_{44} = C_{55} = C_{66} \neq 0$, all other elements are identically zero, and that $2C_{44} \neq C_{11} - C_{12}$. Each case will be considered separately, first showing that C_{11}, C_{12}, and C_{44} are non-zero and independent and then showing that C_{14} and C_{45} are identically zero. Finally, it will be shown that the symmetry of the stiffness functions k_n and k_s leads to equivalence between the symmetry related elastic constants in a cubic systems.

Demonstration that C_{11} is Non-zero

Considering strain path:

$$\varepsilon_1 = \begin{bmatrix} 1 & 0 & 0 \\ 0 & 0 & 0 \\ 0 & 0 & 0 \end{bmatrix} \quad .45$$

and direction $\hat{n}$ parameterized by polar angle, θ, and azimuthal angle, ϕ, the elastic constant C_{11} can be written as the integral:

$$C_{11} = \frac{N_b l^2}{4\pi} \int d\theta \sin(\theta) \int d\phi \left[\begin{array}{c} \left(k_n(\theta,\phi) - k_s(\theta,\phi)\right) \cos^4(\phi)\sin^4(\theta) \\ + k_s(\theta,\phi)\cos^2(\phi)\sin^2(\theta) \end{array} \right] \neq 0 \qquad .46$$

Demonstration that C_{12} is Non-zero

Considering the additional strain path:

$$\varepsilon_2 = \begin{bmatrix} 0 & 0 & 0 \\ 0 & 1 & 0 \\ 0 & 0 & 0 \end{bmatrix} \qquad .47$$

one obtains:

$$C_{12} = \frac{N_b l^2}{4\pi} \int d\theta \sin(\theta) \int d\phi \left[(k_n - k_s)\sin^2(\phi)\cos^2(\phi)\sin^4(\theta) \right] \neq 0 \qquad .48$$

where the angularly dependent stiffness functions have been written simply as k_n and k_s for the sake of brevity.

Demonstration that C_{44} is Non-zero

Using the strain path:

$$\varepsilon_4 = \begin{bmatrix} 0 & 0 & 0 \\ 0 & 0 & 1 \\ 0 & 1 & 0 \end{bmatrix} \qquad .49$$

one obtains:

$$C_{44} = \frac{N_b l^2}{16\pi} \int d\theta \sin(\theta) \int d\phi \left[\begin{array}{c} (k_n - k_s)4\sin^2(\phi)\sin^2(\theta)\cos^2(\theta) \\ + k_s\left(\sin^2(\phi)\sin^2(\theta) + \cos^2(\theta)\right) \end{array} \right] \neq 0 \qquad .50$$

Demonstration that C_{14} *is Identically Zero*

Mixing the normal and shear deformation using the strain paths one obtains:

$$C_{14} = \frac{N_b l^2}{4\pi} \int d\theta \sin(\theta) \int d\phi \left[(k_n - k_s) 4\sin(\phi)\cos^2(\phi)\sin^3(\theta)\cos(\theta) \right] = 0 \qquad .51$$

The stiffness functions k_n and k_s are constructed to possess cubic symmetry (triad axes along $\langle 111 \rangle$) and so also posses mirror symmetry on the $\phi = 0$ plane. The term $\sin(\phi)\cos^2(\phi)$ is antisymmetric in ϕ and so the expression integrates identically to zero.

Demonstration that C_{45} *is Identically Zero*

Mixing shear deformations along different directions using the strain path:

$$\varepsilon_5 = \begin{bmatrix} 0 & 0 & 1 \\ 0 & 0 & 0 \\ 1 & 0 & 0 \end{bmatrix} = \frac{1}{2}\gamma_5 \qquad .52$$

one obtains:

$$C_{45} = \frac{N_b l^2}{8\pi} \int d\theta \sin(\theta) \int d\phi \begin{bmatrix} (k_n - k_s)\sin(2\phi)\sin^2(\phi)\cos^2(\theta) \\ +k_s \sin(2\phi)\sin^2(\theta) \end{bmatrix} = 0 \qquad .53$$

In this expression, $\sin(2\phi)$ is antisymmetric in ϕ and, as with C_{14}, the expression integrates identically to zero.

Demonstration that C_{11}, C_{12}, *and* C_{44} *are Independently Tunable*

For non-isotropic elasticity one requires that $2C_{44} \neq C_{11} - C_{12}$. Using the equations above:

$$C_{11} - C_{12} = \frac{N_b l^2}{4\pi} \int d\theta \sin(\theta) \int d\phi \begin{bmatrix} (k_n - k_s)\cos^2(\phi)\cos(2\phi)\sin^4(\theta) \\ +k_s \cos^2(\phi)\sin^2(\theta) \end{bmatrix} \neq 2C_{44} \qquad .54$$

It can hence be seen by comparison of this with the equation for that C_{11}, C_{12}, and C_{44} must be independent.

34

Symmetry Relationships Between Stiffness Elements

The final task is to show that if k_n and k_s posses cubic symmetry, then the elastic constants also satisfy the cubic symmetry relations so that, for example, $C_{11} = C_{22} = C_{33}$. By possessing cubic symmetry, the stiffness function is invariant under a three-fold rotation about [111] so that:

$$k(\hat{n}) = k(\hat{n} \cdot L) \qquad .55$$

where:

$$L = L_{3[111]} = \begin{bmatrix} 0 & 0 & 1 \\ 1 & 0 & 0 \\ 0 & 1 & 0 \end{bmatrix} \qquad .56$$

is the transformation matrix for a three-fold rotation about [111] axis. Consider imposed normal strain along $\hat{y}$:

$$\varepsilon_2 = \begin{bmatrix} 0 & 0 & 0 \\ 0 & 1 & 0 \\ 0 & 0 & 0 \end{bmatrix} = L \cdot \varepsilon_1 \cdot L^{-1} \qquad .57$$

so that C_{22} is given by:

$$C_{22} = \frac{N_b l^2}{8\pi} \int d\hat{n} \left[(k_n - k_s)(\hat{n} \cdot \varepsilon_2 \cdot \hat{n})^2 + k_s(\hat{n} \cdot \varepsilon_2) \cdot (\hat{n} \cdot \varepsilon_2) \right] \qquad .58$$

Using the symmetry relationship, we can write this in terms ε_1, a normal strain path along $\hat{x}$:

$$C_{22} = \frac{N_b l^2}{8\pi} \int d\hat{n} \begin{bmatrix} (k_n - k_s)\left(\hat{n} \cdot \left(L \cdot \varepsilon_1 \cdot L^{-1}\right) \cdot \hat{n}\right)^2 \\ + k_s\left(\hat{n} \cdot \left(L \cdot \varepsilon_1 \cdot L^{-1}\right)\right) \cdot \left(\hat{n} \cdot \left(L \cdot \varepsilon_1 \cdot L^{-1}\right)\right) \end{bmatrix} \qquad .59$$

Rearranging the order of these matrix products and substituting for $\hat{n}' = \hat{n} \cdot L$ gives:

$$C_{22} = \frac{N_b l^2}{8\pi} \int d\hat{n} \left[(k_n - k_s)(\hat{n}' \cdot \varepsilon_1 \cdot \hat{n}')^2 + k_s(\hat{n}' \cdot \varepsilon_1) \cdot (\hat{n}' \cdot \varepsilon_1) \right] \qquad .60$$

and as $k_n(\hat{n}) = k_n(\hat{n} \cdot L) = k_n(\hat{n}')$ and $k_s(\hat{n}) = k_s(\hat{n} \cdot L) = k_s(\hat{n}')$, and the integral is performed over the full solid angle we see that:

35

$$C_{22} = \frac{N_b l^2}{8\pi} \int d\hat{n} \Big[\big(k_n(\hat{n}') - k_s(\hat{n}') \big) \big(\hat{n}' \cdot \varepsilon_1 \cdot \hat{n}' \big)^2 + k_s(\hat{n}') \big(\hat{n}' \cdot \varepsilon_1 \big) \cdot \big(\hat{n}' \cdot \varepsilon_1 \big) \Big]$$

$$C_{22} = C_{11}$$

.61

A similar approach can be used to prove the equivalence of the other symmetry related stiffness elements; however, this is left as an exercise for the reader.

APPENDIX C. COMPARISON OF ANALYTIC MODEL WITH DEM MODEL

As with the DEM simulation, a simple method for identifying the accessible elastic domain using the analytical model is to randomly sample the parameter space and plot the resulting cloud of elastic properties. The results are shown in Figure Fig. C.1(a). It can be seen that the domain is remarkably similar to that which is accessible by the DEM model presented in Figure 8. Also shown in Fig. C.1(b) is the deviation between the analytic model and the DEM model in both C_{12}/C_{11} and C_{44}/C_{11} for the case where Z>1. It can be seen that deviation of the models is lowest in C_{12}/C_{11} for high α_k and the reverse for C_{44}/C_{11}. It we assume that the deviation between the analytic and DEM models is due to the non-affine internal deformation in the DEM model, then we can see that an optimal choice of model parameters is to choose anisotropy factors a_n and a_s as close to 1 as possible, and choosing a_k to minimize the non-affine deformation of the assembly.
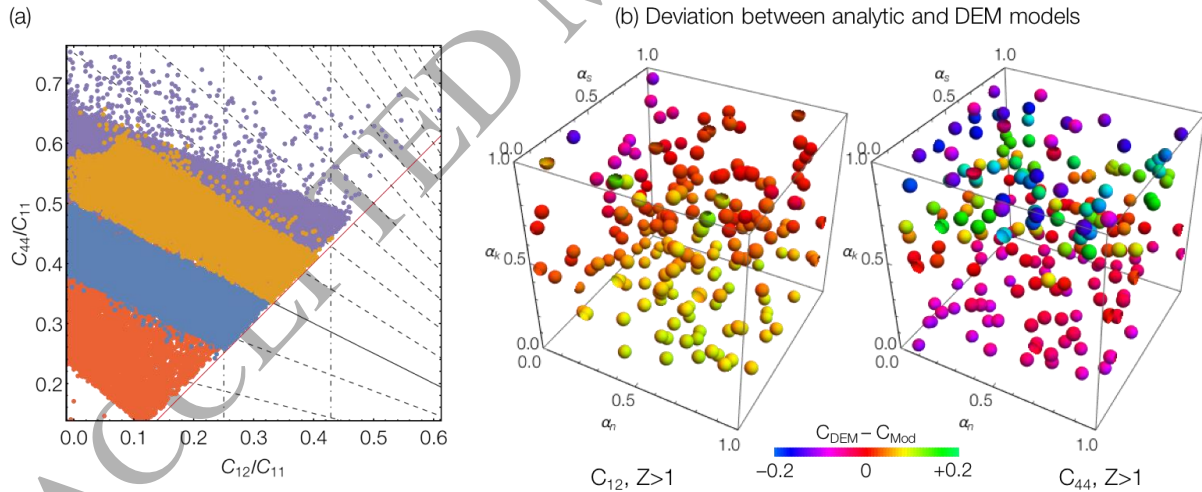

Figure C.1: (a) Domain of elasticity space accessible by spheroid based stiffness interactions demarked by plotting the elasticity from 10,000 randomly sampled points in the input parameter space. The blue and gold data is for the model using stiffness functions used in the DEM model, and it can be seen that the accessible domain is similar to the at in Figure 8 for the DEM model. The purple and orange data is generated using stiffness functions ad before but with the addition of correction terms from the addition of spheroids aligned along the <110> directions. (b) Deviation between the analytic model and DEM simulations plotted at 500 randomly sampled points of the log normalized input parameter space. Red is zero deviation.

APPENDIX D. INSIGHTS FOR EXPANDING THE ACCESSIBLE DOMAIN OF ELASTICITY

The accessible domain of elasticity space is enclosed in one direction by a line of constant Zener ratio and in the other by the Cauchy relationship $C_{12} = C_{44}$. The boundaries of accessible space of the DEM model are parallel to those of the analytic model, but while both models can achieve similar levels of elastic anisotropy, the DEM model can access a region considerably to the right of the $C_{12} = C_{44}$ boundary of the analytic model. That is, the analytic model cannot produce values of $C_{12} - C_{44} > 0$. To examine how the angular distributions of bond stiffness could be revised to push past the boundaries in Z and $C_{12} - C_{44}$, we can examine the integral equations that give rise to these quantities. The Zener ratio is given by:

$$ Z = \frac{2\tilde{C}_{44}}{1 - \tilde{C}_{12}} = \frac{\int d\hat{n}(\chi_n k_n + \chi_s k_s)}{\int d\hat{n}(\gamma_n k_n + \gamma_s k_s)} \tag{.62}$$

where the tilde denotes the dimensionless elastic stiffness element normalized by C_{11} and the functions χ and γ are

$$
\begin{aligned}
\chi_n &= \sin^2(2\theta)\sin^2(\phi) \\
\chi_s &= \cos^2(\theta) - \sin^2(\theta)(2\cos(2\theta)+1)\sin^2(\phi) \\
\gamma_n &= 2\sin^4(\theta)\cos^2(\phi)\cos(2\phi) \\
\gamma_s &= -2\sin^2(\theta)\cos^2(\phi)(\sin^2(\theta)\cos(2\phi)-1)
\end{aligned}
\tag{.63}
$$

If we consider just the case for the Z > 0 model in which k_n peaked along $\langle 111 \rangle$ and k_s along $\langle 100 \rangle$, then to push the boundaries in Z, we wish to maximize the numerator of Z while minimizing its denominator. That is we wish to maximize the overlap of χ and k in the numerator, and minimize overlap of γ and k in the denominator. The functions χ and γ are plotted overlain with their respective stiffness functions in Figure D.1. From these figures it is clear that Z could be increased if k_n was altered so that bonds were stiffer for normal displacements along the $\langle 110 \rangle$ directions, and that k_s was varied to make bond softer in shear along $\langle 110 \rangle$. With the spheroid-based forms of k_n and k_s, it is not possible to independently tune the stiffness of the $\langle 110 \rangle$ directions, and thus the model predicts that the best next iteration of a stiffness function would include the flexibility to tune the stiffness in these directions as well. In the complementary direction the distance from the $C_{12} = C_{44}$ boundary is given by:

$$C_{12} - C_{44} = \int d\hat{n} \left(\zeta_n k_n + \zeta_s k_s \right) \tag{.64}$$

where:

$$\zeta_n = 2\sin^2(\theta)\sin^2(\phi)\left(\sin^2(\theta)\cos^2(\phi) - \cos^2(\theta)\right)$$

$$\zeta_s = \frac{1}{2}\left(\sin^4(\theta)\left(-\sin^2(2\phi)\right) + \sin^2(\theta)\left(2\cos(2\theta)+1\right)\sin^2(\phi) - \cos^2(\theta)\right) \tag{.65}$$

These are also plotted in Figure D.1. The function ζ_n has maxima along the $\langle 110 \rangle$ directions, but is antisymmetric, and so the overlap with k_n integrates to zero. The term ζ_s is negative for all directions, and so the integral of its overlap with k_s is also negative. This means that not only is $\tilde{C}_{12} - \tilde{C}_{44}$ always less than or equal to zero, there is no change that can be made to the stiffness functions that will make $\tilde{C}_{12} - \tilde{C}_{44} > 0$ while still possessing cubic symmetry in k_n and k_s. This makes it all the more remarkable that the DEM model is able to obtain values of $\tilde{C}_{12} - \tilde{C}_{44}$ in excess of 0.1. We attribute this to a not overly redundant bond network permitting non-affine deformation of the assembly.
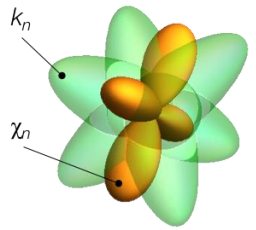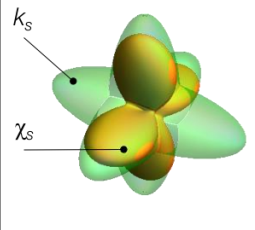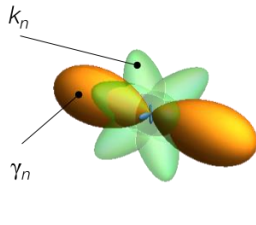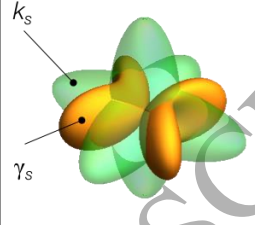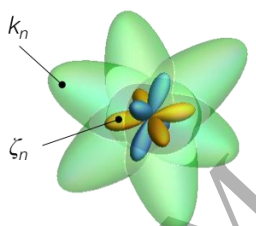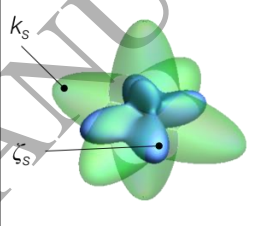
Figure D.1: The overlap kernels for the integrals for F and $\tilde{C}_{12} - \tilde{C}_{44}$ for the Z model. Bond stiffness functions are plotted as a translucent green surface. For the other function positive values are plotted in gold, and negative values in blue. The left-hand column is for the integral of the normal stiffness, and the right column for the shear stiffness. The top row is for the kernels in the integrals of the numerator of Z, the middle row for the terms in it denominator. Expanding the boundary of the accessible domain in Z requires maximizing the top row and minimizing the middle row. The bottom row shows the kernels of the integrals in $\tilde{C}_{12} - \tilde{C}_{44}$. The integral over k_n is identically zero by symmetry, and as function weighting the integral over k_s is everywhere negative $\tilde{C}_{12} - \tilde{C}_{44} \leq 0$, and there is no change to the stiffness functions consistent with the cubic symmetry that will ever make $\tilde{C}_{12} - \tilde{C}_{44}$ positive.

REFERENCES

Andre, D., Jebahi, M., Iordanoff, I., Charles, J.L., Neauport, J., 2013. Using the discrete element method to simulate brittle fracture in the indentation of a silica glass with a blunt indenter. Comput. Meth. Appl. Mech. Eng. 265, 136-147.

Belheine, N., Plasslard, J.P., Donze, F.V., Darve, F., Seridi, A., 2009. Numerical simulation of drained triaxial test using 3D discrete element modeling. Comput. Geotech. 36, 320-331.

Cundall, P.A., 1971. A computer model for simulating progressive, large-scale movements in blocky rock systems, Proceedings of the International Symposium on Rock Mechanics, Nancy, France, pp. 129–136.

Cundall, P.A., Strack, O.D.L., 1979. Discrete Numerical-Model for Granular Assemblies. Geotechnique 29, 47-65.

Evans, T.M., Frost, J.D., 2007. Shear Banding and Microstructure Evolution in 2D Numerical Experiments, Advances in Measurement and Modeling of Soil Behavior, p. GSP 173.

Evans, T.M., Frost, J.D., 2010. Multiscale investigation of shear bands in sand: Physical and numerical experiments. Int. J. Numer. Anal. Methods Geomech. 34, 1634-1650.

Evans, T.M., Valdes, J.R., 2011. The microstructure of particulate mixtures in one-dimensional compression: numerical studies. Granul. Matter 13, 657-669.

Fakhimi, A., Carvalho, F., Ishida, T., Labuz, J.F., 2002. Simulation of failure around a circular opening in rock. Int J Rock Mech Min 39, 507-515.

Hahn, M., Bouriga, M., Kroplin, B.H., Wallmersperger, T., 2013. Life time prediction of metallic materials with the Discrete-Element-Method. Comput. Mater. Sci. 71, 146-156.

Hedjazi, L., Martin, C.L., Guessasma, S., Della Valle, G., Dendievel, R., 2012. Application of the Discrete Element Method to crack propagation and crack branching in a vitreous dense biopolymer material. International Journal of Solids and Structures 49, 1893-1899.

Jacobson, D.E., Valdes, J.R., Evans, T.M., 2007. A numerical view into direct shear specimen size effects. Geotech. Test. J. 30, 512-516.

Jebahi, M., Andre, D., Dau, F., Charles, J.L., Iordanoff, I., 2013. Simulation of Vickers indentation of silica glass. J. Non-Cryst. Solids 378, 15-24.

Johnson, J.B., Hopkin, M.A., 2005. Identifying microstructural deformation mechanisms in snow using discrete-element modeling. J. Glaciol. 51, 432-442.

Kosteski, L., D'Ambra, R.B., Iturrioz, I., 2012. Crack propagation in elastic solids using the truss-like discrete element method. Int. J. Fract. 174, 139-161.

Le, B.D., Dau, F., Charles, J.L., Iordanoff, I., 2016. Modeling damages and cracks growth in composite with a 3D discrete element method. Compos Part B-Eng 91, 615-630.

Lobo-Guerrero, S., Vallejo, L.E., 2005. Crushing a weak granular material: experimental numerical analyses. Geotechnique 55, 245-249.

Maheo, L., Dau, F., Andre, D., Charles, J.L., Iordanoff, I., 2015. A promising way to model cracks in composite using Discrete Element Method. Compos Part B-Eng 71, 193-202.

Martin, C.L., Camacho-Montes, H., Olmos, L., Bouvard, D., Bordiaz, R.K., 2009. Evolution of Defects During Sintering: Discrete Element Simulations. J. Am. Ceram. Soc. 92, 1435-1441.

Ning, Z., Khoubani, A., Evans, T.M., 2015. Shear wave propagation in granular assemblies. Comput. Geotech. 69, 615-626.

O'Sullivan, C., 2011. Particulate Discrete Element Modelling: A Geomechanics Perspective. Taylor & Francis.

Potyondy, D.O., Cundall, P.A., 2004. A bonded-particle model for rock. Int J Rock Mech Min 41, 1329-1364.

Roux, J.-N., Chevoir, F., 2005. Discrete numerical simulation and the mechanical behavior of granular materials. Bulletin de Liaison des Laboratoires des Ponts et Chaussees 254, 109-138.

Saad, Y., Schultz, M.H., 1986. Gmres - a Generalized Minimal Residual Algorithm for Solving Nonsymmetric Linear-Systems. Siam J Sci Stat Comp 7, 856-869.

Simmons, G., Wang, H., 1971. Single crystal elastic constants and calculated aggregate properties: a handbook. M.I.T. Press.

Truszkowska, A., Yu, Q., Greaney, P.A., Evans, T.M., Kruzic, J.J., 2017. Developing a Crystal Plasticity Model for Metallic Materials Based on the Discrete Element Method. MRS Advances, 1-6. doi:10.1557/adv.2017.1430.

Verlet, L., 1967. Computer Experiments on Classical Fluids .I. Thermodynamical Properties of Lennard-Jones Molecules. Phys Rev 159, 98-103.

Wang, Y.H., Xu, D.P., Tsui, K.Y., 2008. Discrete element modeling of contact creep and aging in sand. J. Geotech. Geoenviron. Eng. 134, 1407-1411.

Yun, T.S., Evans, T.M., 2011. Evolution of at-rest lateral stress for cemented sands: experimental and numerical investigation. Granul. Matter 13, 671-683.

Zhao, S.W., Evans, T.M., Zhou, X.W., Zhou, S., 2017. Discrete element method investigation on thermally-induced shakedown of granular materials. Granul. Matter 19, 11.

Zhu, H.P., Zhou, Z.Y., Yang, R.Y., Yu, A.B., 2007. Discrete particle simulation of particulate systems: Theoretical developments. Chem. Eng. Sci. 62, 3378-3396.

Zhu, H.P., Zhou, Z.Y., Yang, R.Y., Yu, A.B., 2008. Discrete particle simulation of particulate systems: A review of major applications and findings. Chem. Eng. Sci. 63, 5728-5770.